Particulate Trace Element Export in the North Atlantic (GEOTRACES GA01 Transect, GEOVIDE Cruise)

Nolwenn Lemaitre, Hélène Planquette, Frank Dehairs, Frédéric Planchon, Géraldine Sarthou, Morgane Gallinari, Stéphane Roig, Catherine Jeandel, Maxi Castrillejo

ACS Earth and Space Chemistry
Article In Press
Acceptation date : 2020
https://doi.org/10.1021/acsearthspacechem.0c00045
https://archimer.ifremer.fr/doc/00656/76810/

Particulate Trace Element Export in the North Atlantic (GEOTRACES GA01 Transect, GEOVIDE Cruise)

Lemaitre Nolwenn [1, 2, 3, *] , Planquette Helene [2], Dehairs Frank [3], Planchon Frederic [2], Sarthou Geraldine [2], Gallinari Morgane [2], Roig Stéphane [2], Jeandel Catherine [4], Castrillejo Maxi [5]

[1] Institute of Geochemistry and Petrology, ETH-Zurich, Clausiusstrasse 25, 8092 Zurich, Switzerland
[2] CNRS, Université de Brest, IRD, Ifremer, LEMAR, Technopôle Brest-Iroise, 29280 Plouzané, France
[3] Analytical, Environmental, and Geo-Chemistry, Vrije Universiteit Brussel, Pleinlaan, 1050 Brussels, Belgium
[4] LEGOS, Université de Toulouse (CNRS/CNES/IRD/UPS), Observatoire Midi Pyrénées, 31400 Toulouse, France
[5] Laboratory of Ion Beam Physics, ETH-Zurich, Otto Stern Weg 5, 8093 Zurich, Switzerland

* Corresponding author : Nolwenn Lemaitre, email address : nolwenn.lemaitre@erdw.ethz.ch

Abstract :

Vertical export of particulate trace elements (pTEs) is a critically underconstrained aspect of their biogeochemistry. Here, we combine elemental analyses on large (>53 μm) particles and 234Th measurements to determine downward export fluxes from the upper layers (40–110 m) of pTEs (Al, Cd, Co, Cu, Fe, Mn, Ni, P, Ti, V, Zn) and mineral phases (lithogenic, Fe- and Mn-oxides, calcium carbonate, and opal) in the North Atlantic along the GEOVIDE transect (Portugal–Greenland–Canada; GEOTRACES GA01 cruise). The role of lithogenic particles in controlling TE fluxes is obvious at proximity of the Iberian margin where the highest pTE export fluxes were estimated (up to 3912 μg/m2/d for pFe). However, high lithogenic and pTE fluxes are also observed up to 1700 km off this margin in the west European and Icelandic basins (up to 931 μg/m2/d for pFe). The lowest pTE export fluxes are determined in the Labrador Sea (as low as 501 μg/m2/d for pFe). High Mn- and Fe-oxide fluxes are estimated at the open ocean stations, suggesting that authigenic particles are an important vector of pTEs. All along the transect, biogenic particles also drive the pTE export fluxes, as shown by the similar pTE/POC ratios between exports and phytoplankton quotas. The shortest residence times (dissolved + particulate) are generally observed where lithogenic particles control the pTE fluxes (as low as 2 days for Fe) whereas pTEs seem to be longer retained when the contribution of biogenic particles become greater (residence times up to 147 days for Fe).

Keywords : particulate trace elements, export fluxes, multiple carrier phases, residence times, GEOTRACES

1. INTRODUCTION

Bioactive trace elements (TEs: Cd, Co, Cu, Fe, Mn, Ni, Zn, etc.) are important for the marine primary productivity [1], as they are required for numerous metabolic processes [2,3]. Sometimes in line with other bioactive trace elements, depleted Fe concentrations in the surface waters can limit the phytoplankton, thus influencing the community structure and, as a result, the overall marine carbon cycle [4,5]. Therefore, the quantification of biogeochemical processes regulating the internal cycle of TEs is essential to better understand the carbon cycle and in particular the biological carbon pump [6,7].

Many TEs reach the ocean through particles, either via atmospheric dusts [8], rivers [9], margins [10] or sediments [11]. Marine particles also participate in the removal of TEs, either through scavenging onto particle surfaces [12], precipitation of authigenic minerals such as barite [13–15] and Mn-Fe oxyhydroxides [16], or sinking to the deep ocean due to lithogenic and biogenic ballast minerals [17–19]. Small (suspended; 1-53µm diameter) particles mainly trap TEs via scavenging, though they have been shown to slowly sink after coagulation to other particles [20,21]. Large (sinking; >53µm diameter) particles export TEs from the biologically active upper water column down to the interior ocean [22], with the remineralization length scale controlling the release of TEs into solution and their subsequent return to the surface. Earlier studies have revealed that particulate phosphorous (pP), nickel (pNi), zinc (pZn) and organic carbon (POC) are remineralized faster than particulate iron (pFe) because of a stronger scavenging of dissolved Fe onto particles [23,24]. Thus, particle-solute interactions determine the residence times of TEs in the water column. However these residence times are presently not well known because of scarce estimates of TE inventories and fluxes into or out of the water column [25]. Despite an increasing number of studies addressing TE export, this process remains still poorly understood [23,26,35,36,27–34]. Besides the strong temporal and spatial variability, another reason likely resides in the difficulty in measuring particulate trace element (pTE) fluxes, as TEs are

present at very low concentrations in the ocean and are easily prone to contamination. Sediment traps are used to directly quantify the pTE export fluxes [29,30,37,38] but their deployment tends to be time- and effort-intensive. They also can be biased because of lateral advection or because of possible TE contamination from the preservative solution added into the cups to avoid zooplankton and microbial activities[39]. One alternative for determining particulate export fluxes is the clean but indirect ^{234}Th-^{238}U method [40–42]. ^{234}Th is a highly particle-reactive element with a short half-life (t ½ = 24.1 days) compared to its radioactive parent ^{238}U (t ½ = 4.47 billion years). While both isotopes are usually at secular equilibrium in subsurface waters, a deficit of ^{234}Th relative to ^{238}U can be observed in the upper ocean, where sinking particles carry ^{234}Th downward. This deficit of ^{234}Th relative to ^{238}U can be converted into an elemental export flux when multiplied with the ratio of the element to ^{234}Th (element:^{234}Th hereafter) in the particulate material at a given depth [34,41]. This method has the benefit to allow flux determination at multiple stations and for a large suite of elements and mineral phases.

The presence of lithogenic and biogenic minerals, as well as oxyhydroxides, are identified as phases liable to control the settling of particles with depth [19]. In the temperate north Atlantic, advection of lithogenic material from continental margins and pronounced seasonal phytoplankton blooms strongly enhance the pTE distributions and downward export fluxes [43–47]. However, occasional lack of nutrients such as dissolved iron (dFe) [48] can limit the primary productivity, the magnitude of the downward fluxes and thus the strength of the biological carbon pump [5,49,50]. This is well illustrated in the subtropical north Atlantic, which is characterized by oligotrophic conditions leading to low primary production [51] and to low export fluxes of POC [52,53] and pTEs [43]. In this region, exports of POC [54–58] and pTEs [28] show episodic fluctuations along the season due to nutrient and/or light limitations but also due to lithogenic inputs mainly originating from margins or associated with atmospheric dust depositions [28,43,44,59]. The more productive subpolar Atlantic is characterized by lower lithogenic inputs

because of the decreasing influence of the Saharan dust plume [43]. Nevertheless, lateral supplies of lithogenic material from continental shelves have been reported and could enhance the export fluxes [28,34].

In this study, we aim to better understand the processes controlling the TE distributions in the upper layers of the North Atlantic Ocean by focusing on particulate TE export. The different particulate substrates (authigenic, lithogenic and biogenic) liable to carry the pTEs are investigated and the export efficiencies are evaluated by estimating the residence times of TEs within the upper ocean.

2. METHODS

2.1. Biogeochemical characteristics of investigated stations

Fieldwork was conducted on board the French *R/V Pourquoi Pas?* along the GEOTRACES GA01 section during the GEOVIDE expedition (Fig. 1). The cruise was carried out in May-June 2014. We sampled a total of 11 stations located in five different biogeochemical domains described in details in Lemaitre et al. (2018) [60] and in Table 1. Briefly, the Iberian basin was sampled after the spring bloom and was characterized by a low primary productivity (PP) [61]. Station #13 had the highest proportion of cyanobacteria (12% of phytoplankton abundance) of the all transect [62]. Particulate organic carbon (POC) export was high at Station #1 while low at Station #13, reflecting the low nutrient availability in subtropical waters [60]. The west European (Stations #21 and #26) and Icelandic (Stations #32 and #38) basins were sampled during the bloom development and were the most productive areas with the highest PP observed along the transect [60]. Diatoms dominated the phytoplankton community (41% of phytoplankton abundance) but dinoflagellates and haptophytes (including coccolitophorids) also contributed significantly in the west European basin (~20% of phytoplankton abundance [62]). Conversely, nano-phytoplankon and mainly haptophytes dominated the community in the Icelandic basin.

High POC exports were determined in both basins and particularly at Station #32 [60]. The Irminger basin (Stations #44 and #51) was sampled close to the bloom maximum and PP values were high, with a clear dominance of diatoms (between 55 and 77% of phytoplankton abundance [62]). Because of the accumulation of biomass in the surface waters, POC export fluxes were low, with Station #44 having the lowest one of the entire cruise [60]. The Labrador basin (Stations #64, #69 and #77) was sampled after the PP peak, at the onset of the bloom decline [60]. Productivity was relatively low compared to the other studied basins. Diatoms were also dominating, contributing up to 62% of the phytoplankton abundance [62]. POC export fluxes were relatively high, likely because of the increasing number of rapidly sinking particles [60].

2.2. Particle sampling

Total ^{234}Th activities were determined from 4L unfiltered seawater sampled with 12L Niskin bottles mounted on CTD rosette and were processed following the method of Pike et al. (2005) [63]. Samples were acidified and spiked with a ^{230}Th yield monitor in order to estimate the ^{234}Th recovery during sample processing. After a 12h equilibration, pH was increased and $KMnO_4$ and $MnCl_2$ solutions were added. After a further 12h equilibration, samples were filtered on quartz-microfiber discs (QMA, Sartorius, nominal porosity=1 µm, diameter=25 mm) and the ^{234}Th activities were measured on-board using a low-level beta counter (RISØ®, Denmark). Residual beta activities were measured ~6 months after the cruise after which samples were processed for Th recoveries using ^{229}Th as a second yield tracer. Export fluxes of ^{234}Th were then calculated using a 1-D box model [64] under steady state assumptions and neglecting advection and diffusion [41]. Export fluxes of ^{234}Th are presented in Lemaitre et al (2018) [60].

Particulate matter for biogenic silica (BSi), calcium carbonate ($CaCO_3$) and pTE analyses was collected on the same *in-situ* pump (Challenger Oceanics® and McLane® pumps, ISP) filter, whereas particles for POC were collected using a separate filter holder. The later was mounted either on a second flow path when modified McLane ISP heads were used, or with a separate

ISP unit [60] attached 10 to 50 m apart from the ISP dedicated to TEs (see Table S1). Particulate ^{234}Th activity in the large size particle fraction (LSF, >53µm) was determined on particles collected with each ISP system (Fig. S1).

Particulate organic carbon (POC) LSF was collected on a 53-µm mesh polyester screen (Petex), which was cut into quarters. Particles present on one quarter of the Petex screen were rinsed-off using 0.45 µm filtered seawater obtained during the cruise and subsequently collected on a silver filter (SterliTech, nominal porosity=0.45 µm, diameter=25 mm) for one quarter, and on a GF/F filter (Whatman, nominal porosity=0.7 µm, diameter=25 mm) for another quarter, before being Beta-counted on board. Back in the home laboratory, samples were prepared for POC analyses: filters were fumed with HCl vapor, dried, packed in pre-combusted silver cups and analysed with an elemental analyser (EA-IRMS, Delta V Plus, Thermo Scientific). More details on POC and particulate ^{234}Th (p^{234}Th) analyses can be found in Lemaitre et al. (2018) [60].

Particulate matter for BSi, $CaCO_3$ and pTE determinations was filtered on a 142mm-diameter 53-µm mesh polyester screen (Petex) for the LSF upstream of a 142mm-diameter 0.8-µm polyethersulfone filter (Supor®) for the small size particle fraction (SSF). Before use, filters were soaked in 1.2M HCl (Suprapur grade, Merck), heated overnight at 60°C and subsequently rinsed with Milli-Q grade water. On board, filters were processed under a laminar flow unit within a customized clean "bubble" to prevent contamination. Before and after the ISP recoveries, pump heads were protected with plastic bags to minimize contamination. After pump recoveries, filter heads were dismantled and carried inside the clean bubble.

Using a clean ceramic scalpel, one quarter of the Petex screen, dedicated to p^{234}Th and BSi analyses, was cut out. Particles were washed off the Petex screen using 0.45-µm filtered seawater obtained during the cruise. Particles were then collected on polycarbonate filters (PC; Nuclepore®, porosity=0.4µm, diameter=25mm) mounted on a polysulfone filtration unit.

Filters were left to dry at room temperature inside the laminar flow unit and subsequently prepared for Beta counting. Activities of $p^{234}Th$ were also determined on a second quarter of the Petex screen: particles were washed off, using the 0.45-µm filtered seawater, and collected on a polyethersulfone filter (Supor®, porosity=0.45 µm, diameter=25 mm) mounted on a Nalgene filtration unit (Fig. S1). Because Beta counting of samples is probably incompatible with trace metal clean stringent conditions, the two last quarters of the Petex screen, dedicated to pTEs, particulate calcium (pCa) and sodium (pNa), were stored in a clean petrislide (Pall Gelman) and kept at -20°C until sample processing and analysis in the home laboratory. Since Supor filters with the SSF were not Beta counted, there are no data for the SSF $p^{234}Th$ activity.

2.3. Particulate matter analyses

The methods used here have been approved during a GEOTRACES intercalibration exercise and our elemental concentrations have been submitted to the GEOTRACES Intermediate Data Product (IDP) 2021. The concentrations obtained from ISP sampling (this study) have been compared to those obtained by GO-FLO sampling at the same locations (from Gourain et al., 2019 [65] and from Planquette et al., personal communication, 2019). Both datasets were obtained after using exactly the same digestion and analytical methods. Although similar element profiles were obtained from both datasets, highlighting data consistency, we note that pTE concentrations obtained from ISP sampling were generally lower than those obtained from GO-FLO bottles. This discrepancy could possibly result from particle washout during ISP recovery, since our ISPs were not systematically equipped with anti-washout systems, or due to some loss when transferring particles from the Petex screens to other filters (see above). To limit these effects, our study focuses on elemental ratios and on element:^{234}Th ratios, rather than on concentrations or activities.

190 2.3.1. Trace and major elements

191 In the home laboratory the two remaining quarters of Petex screen saved for pTEs, pCa and
192 pNa analyses were washed off with 0.45-µm filtered, low TE surface seawater collected during
193 the GEOVIDE cruise (Station #77, 40m, filtered through a Supor filter, 0.45µm) and
194 subsequently collected on acid cleaned 47-mm diameter mixed cellulose esters filters (MF-
195 Millipore® filters, 0.8µm), using Nalgene® filtration units (Fig. S1). Then, filters were
196 processed following the protocol of Planquette and Sherrell (2012) [66]. Briefly, one half of the
197 MF filter was kept in a clean petrislide while the other half was placed along the wall of an
198 acid cleaned Teflon vial (Savillex®) and digested with a HNO_3 8 M - HF 2.3 M mix solution
199 (Ultrapur and Suprapur grades, respectively, Merck®), refluxing at 130°C during 4h. After
200 gentle evaporation close to near dryness, 200 µL of concentrated HNO_3 (Ultrapur grade,
201 Merck) was added in order to drive off the fluorides. The residue was brought back into solution
202 with 0.32M HNO_3 spiked with 1 µg/L of indium and stored in acid cleaned centrifuge tubes
203 (Corning®). Measurements of pTEs were performed using a sector field inductively coupled
204 mass spectrometer (SF-ICP-MS, Element 2, Thermo). External calibration curves were run at
205 the start, middle and end of the sequence. The precision and accuracy of our measurements
206 were assessed by analysing the certified reference material (CRM) BCR-414. Recoveries were
207 typically within 10% of the certified values and the precision, given by the relative standard
208 deviation of the five CRM analyses, was between 0.2 and 24% depending on the element (Table
209 2). Gourain et al. (2019) analysed two other CRM (PACS-3 and MESS-4) by using the exact
210 same analytical method and found similar accuracy and precision results [65]. The reproducibility
211 of our analyses was assessed by analytical replicates of 17 samples and differences between
212 replicates were less than 6% from the mean value.

213 Aluminium (Al) is usually used as a tracer of lithogenic particles because of its high crustal
214 abundance (Upper Continental Crust or UCC Al = 8.04% by weight [67]) and its stable

concentrations among lithogenic sources. However, Al has been shown to be removed from the surface waters via scavenging onto particles, especially diatom cells [68]. During GEOVIDE, scavenging onto sinking opal-containing particles was defined as a sink for Al, especially in the Irminger and Labrador basins where diatoms dominate the phytoplankton community [69]. Removal of aluminium via other types of particles (i.e. carbonates, lithogenics, organics, fecal pellets) was not observed in this study, although it cannot be excluded [69]. Using Al as a lithogenic tracer can thus be questioned, especially for the Irminger and Labrador basins. Another lithogenic tracer that can be used is titanium (Ti) but it is less abundant in the UCC (UCC Ti=0.3% [67]) and its concentrations strongly vary between geological materials. We thus calculated the lithogenic mass (litho) using both tracers:

$$\text{Litho } (\mu g/L) = (pAl \times 27 \times 10^{-6}) / 0.0804 \quad (1)$$

$$\text{or Litho } (\mu g/L) = (pTi \times 47.9 \times 10^{-6}) / 0.003 \quad (2)$$

where *pAl* and *pTi* are the particulate Al and Ti concentrations in pmol/L; *0.0804* and *0.003* are the mass fractions of Al and Ti in the UCC; and *27* and *47.9* are the molar masses of Al and Ti in g/mol, respectively.

The GEOVIDE transect, and the north Atlantic in general, is characterized by multiple lithogenic sources (atmospheric, sediment or continental inputs) with different geological characteristics. For example, basaltic rocks present close to Iceland and Greenland have a different Ti concentration than gabbro from the Iberian margin, potentially leading to wrong lithogenic estimations. The flux estimates of MnO_2, $Fe(OH)_3$ and $CaCO_3$ are lower, if not negative, when Ti is used to correct the lithogenic fraction (Fig. S2). We believe that Ti significantly overestimates the lithogenic fraction when its contribution is low (i.e. at all stations except close to the Iberian margin). In the following, we therefore use Al-calculated fluxes, yet keeping in mind that our mineral fluxes might be overestimated, especially in diatom-rich areas like the Irminger and Labrador basins.

Oxyhydroxides of Fe and Mn were calculated by subtracting Fe and Mn associated with lithogenic and biogenic materials from total Fe and Mn. Assuming that Fe oxyhydroxides are ferrihydrite ($Fe(OH)_3$ or Fe-oxides hereafter) and Mn oxyhydroxides are birnessite (MnO_2 or Mn-oxides hereafter), with formula weights 106.9 g $Fe(OH)_3$/mol Fe and 86.9 g MnO_2/mol Mn [70], it is possible to calculate:

$$Fe(OH)_3\ (\mu g/L) = [pFe - (pAl \times 0.21) - (POC \times 0.042)] \times 106.9 \times 10^{-3} \quad (3)$$

$$MnO_2\ (\mu g/L) = [pMn - (pAl \times 0.00367) - (POC \times 0.003)] \times 86.9 \times 10^{-3} \quad (4)$$

where p*Fe*, *pAl* and *pMn* are the total particulate concentrations in nmol/L; POC is the particulate organic carbon concentration in µmol/L; *0.21* and *0.00367* are respectively the UCC pFe:pAl and pMn:pAl ratios in mol/mol [67]; 0.042 and 0.003 are respectively the average Fe:C and Mn:C quota of bulk phytoplankton in nmol/µmol in the North Atlantic (Table 5 in Twining et al., 2015 [71]).

Analyses of pCa and pNa were made using an inductively coupled plasma atomic emission spectrometer (ICP-AES, ULTIMA 2, Horiba Jobin Yvon). As for pTEs, the accuracy and precision were assessed by analysing the CRM BCR-414 (Table 2). Recovery for pCa reached 80%, keeping in mind that only an indicative value for the CRM reference is available. Replicate analyses were made for 6 samples and differences from the mean value averaged 1.3 and 1.2% for pCa and pNa, respectively. As a mineral forming the shells of coccolithophorids, pteropods or foraminifers, we estimate the calcium carbonate ($CaCO_3$) concentrations by correcting for sea-salt and lithogenic Ca:

$$[Ca]_{CaCO3}\ (\mu g/L) = [pCa - (Ca:Na)_{SW} \times pNa - (Ca:Al)_{UCC} \times pAl] \times 100.1 \quad (5)$$

where *pCa*, *pNa* and *pAl* are respectively the total particulate calcium, sodium, and aluminium concentrations in µmol/L; $(Ca:Na)_{SW}$ is equal to 0.022 mol/mol and represents the mean

seawater ratio [72]; $(Ca:Al)_{UCC}$ is equal to 0.251 mol/mol and represents the mean UCC ratio [67]; *100.1* is the molar mass of $CaCO_3$ in g/mol.

2.3.2. Biogenic silica and opal

Following the method of Ragueneau et al. (2005), BSi concentrations were estimated using an alkaline digestion with correction of the lithogenic silica (LSi) [73]. A 25mm diameter Nuclepore filter (carrying the LSF) previously counted for Beta activity was inserted in a polymethylpentene centrifuge tube and digested with a 0.2 M NaOH solution (Merck) at 95°C for 1h. After cooling, the pH was neutralized by adding 1 M HCl (Analar Normapur, Merck) and the supernatant was separated from the remaining suspended material by centrifugation. Silicic acid concentrations were determined following an automated acid/molybdate colorimetric method [74], using an AutoAnalyzer3 Bran&Luebbe®. Dissolved aluminium released during the digestion process was determined by fluorimetric analysis of an Aluminum-Lumogallion complex (fluorimeter MITHRAS LB 940) [75]. At the end of the digestion, all the BSi is converted into silicic acid, but some lithogenic Si may have dissolved as well, inducing a bias in the BSi concentration. This bias was resolved by applying a second digestion, similar to the first one, allowing the determination of a Si:Al ratio exclusively related to the lithogenic material present in the samples. As a mineral forming the shells of diatoms, sponges or radiolarians, we estimate the mass of opal assuming a hydrated form of silica: $SiO_2.(0.4\ H_2O)$ [76], or 67.2 g opal/mol BSi:

$$\text{Opal } (\mu g/L) = ([Si_1] - [Al_1] \times (Si:Al)_2) \times 67.2 \qquad (6)$$

where $[Si_1]$ and $[Al_1]$ are the concentrations of silicic acid and aluminium determined during the first digestion in µmol/L; $(Si:Al)_2$ is the ratio of the concentrations of silicic acid and aluminium determined during the second digestion; and 67.2 is the molar mass of opal in g/mol.

2.4. Component:^{234}Th ratios and export fluxes

Trace element and mineral (lithogenics, Fe- and Mn-oxides, $CaCO_3$, opal) export fluxes were determined using the ^{234}Th-based approach by multiplying the TE:^{234}Th or mineral:^{234}Th ratio of sinking particles with the total ^{234}Th export flux [60], both determined at the same depth:

$$\text{Component export flux} = (\text{component}:^{234}\text{Th})_{\text{particulate}} \times {}^{234}\text{Th flux} \quad (7)$$

with *component* being either a TE or a mineral phase.

As we do not have p^{234}Th activities available for the SSF, we only consider the component:^{234}Th ratios from the LSF in this study. Large particles (>53µm) are generally assumed to represent the sinking particulate matter and are thus responsible for the particulate export flux [77–79]. Using the component:^{234}Th ratios from the LSF to calculate export fluxes is the most common approach [36,80–83]. However, recent studies have shown that the SSF could also contribute to the export flux of particulate carbon or nitrogen in oligotrophic regions [20,21,84]. Black et al. (2019) reported no significant differences in SSF and LSF pP:^{234}Th, pCo:^{234}Th and pCd:^{234}Th ratios contrasting with the higher pMn:^{234}Th ratios in the LSF compared to the SSF, leading to a greater contribution of the LSF to the total pMn flux[36].

Vertical export fluxes were determined at the depth where total ^{234}Th is back to secular equilibrium with ^{238}U (equilibrium depth or Eq hereafter; Table 3). The ^{234}Th export at Eq represents the fully-integrated depletion of total ^{234}Th in the upper waters [60]. To collect particles, three to four depths were sampled per ISP in the upper 150m while in that same depth range, Niskin casts sampled nine depths. Because of this difference of depth resolution we use an interpolation method to estimate the component:^{234}Th ratios for the layer between surface and Eq. The depth-weighted average (DWA) was chosen as this method yields similar TE:^{234}Th or mineral:^{234}Th ratios than those obtained from sediment traps [31] (DWA; element:^{234}Th=$[\Sigma(\text{element}_i \times Z_i) / \Sigma(Z_i)] / [\Sigma(^{234}\text{Th}_i \times Z_i) / \Sigma(Z_i)]$ where Z_i are the depth intervals

sampled above Eq). Uncertainties of ratios and fluxes were obtained using error propagation law.

2.5. Residence times

We also investigated the total residence time (τ) of TEs, which was obtained by dividing the TE inventory within a specific reservoir by the TE flux into or out of this reservoir, thereby assuming steady state with removal rates equalling supply rates (Equation 8). We focused on total (dissolved+particulate) residence time (τ_{total}) within the surface-Eq layer depth (Table 5) and we considered the particulate export flux as the main output flux of TE from the upper ocean. Advective and diffusive circulation fluxes are generally slow processes compared to the vertical export processes and were neglected here [25,35]. However these processes have been shown to have impact, though limited, on measured ^{234}Th export fluxes along the GEOVIDE transect [60], and therefore τ_{total} of TE might represent a higher end estimation in the present study.

$$\tau = \frac{total\ TE\ inventory}{particulate\ TE\ export\ flux} \qquad (8)$$

with the particulate TE export flux in µg/m^2/d at Eq (from this study), and the total TE inventory in µg/m^2 obtained by summing the particulate (>0.45 µm) and dissolved (<0.45 µm) TE phases, both being collected using GO-FLO bottles (Planquette et al., personal communication, 2019 and [65,69,85]). Inventories were calculated using a depth-weighted integration in the surface-Eq layer. Uncertainties in Table 5 represent the highest deviation between the residence time obtained at Eq and those obtained at Eq+20m or Eq-20m (20m being the average error on the determination of the Eq depth).

3. RESULTS

3.1. Activities of $p^{234}Th$ and concentrations of TEs, lithogenic, authigenic and biogenic phases in the large size fraction (>53µm)

Distributions of $p^{234}Th$ vary along the transect (Fig. S3, Table S1) with the lowest activities being determined in the Iberian basin (as low as 0.006 dpm/L in subsurface of Station #1) and the highest in surface waters of the Irminger basin (up to 0.2 dpm/L in surface of Station #51). In general, activities are high in surface and decrease with depth but some subsurface maxima also occur, such as at 100m of Station #64 where activities reach 0.16 dpm/L.

As shown in Figure S3 and Table S1, >53µm concentrations vary between elements, with values ranging from 10^{-6} to 10^{1} nmol/L in the suite of Cd, Co < Cu, Mn, Ni, Ti, Zn < Fe < Al, P. Similarly to $p^{234}Th$ activities, concentrations and distributions also vary significantly for each pTE along the transect, like those of the lithogenic, authigenic and biogenic phases.

Concentrations of pAl or lithogenic material, like that of pFe and pTi, which are known to be associated with lithogenic material, generally increase with depth and are highest at proximity of the Iberian margin (Station #1) reaching up to 15 nmol/L, 5.2 µg/L, 3.2 nmol/L and 0.2 nmol/L at 550m respectively. Similarly, pMn and pZn show maximal concentrations over the transect at 550m at Station #1 (0.05 and 0.9 nmol/L, respectively) though high concentrations are also observed at 100m at Station #64 (0.03 and 0.07 nmol/L, respectively) like pCd, pCu, pNi and pV (7.1 pmol/L, 0.04, 0.02 and 0.05 nmol/L, respectively; Table S1). Lithogenic material is also strongly enriched at 100m at Station #64 and 200m at Station #77 (> 0.8 µg/L). Except for these stations located closer to margins, concentrations of lithogenic material are low, averaging 0.2 µg/L.

Particulate Cd, Co and P are characterized by biogenic distributions, with higher concentrations in surface waters, especially in the productive west European basin (Stations #21 and #26). Other pTEs are characterized by high surface concentrations such as pV and pZn in the

Irminger and Labrador basins or pCd, pCu, pFe pNi and pZn in the west European and Icelandic basins. These coincide with elevated concentrations of both opal and $CaCO_3$ in the upper 100m, where they are produced: highest $CaCO_3$ concentrations mainly occur within the west European and Icelandic basins (up to 14 µg/L) whereas highest opal concentrations occur within the west European, Irminger and Labrador basins (up to 95 µg/L). In general, both biogenic phases display nutrient-like profiles with highest concentrations in surface waters, but deeper $CaCO_3$ maxima occur at Station #32 at 100m, Station #38 at 60m and Station #64 at 100m while deeper opal maxima occur at Stations #38 and #64 at 100m.

Slight increase of pFe, pMn, pCd, pCo, pCu, pNi and pZn concentrations are observed in subsurface, such as at 60m and 100m at Station #64, in the upper 200m at Stations #32 and #38 and below 100m at Station #26. Iron and manganese oxide contents follow similar trends. Both authigenic minerals are obtained after correction of the contribution of lithogenic and biogenic fractions, and therefore show low concentrations along the section, with exceptions at the depths cited just above. At 60m at Station #64, $Fe(OH)_3$ and MnO_2 concentrations reach 0.16 and 0.003 µg/L respectively, but are also relatively high at 100m, coinciding with elevated lithogenic contents (0.05 and 0.002 µg/L respectively). High $Fe(OH)_3$ concentrations are also observed in the upper 200m of the Icelandic basin (from 0.01 to 0.03 µg/L at Stations #32 and #38) while high MnO_2 concentrations are seen below 100m of Station #26 (up to 0.002 µg/L). Overall, our >53µm pTE concentrations are comparable with those of the world ocean literature [31,36,86]. If we compare more closely to data from the GA03 cruise, which also took place in the North Atlantic (GEOTRACES IDP2017 [87]), our concentrations of pP are slightly higher, reaching 24 nmol/L during GEOVIDE (4.7 nmol/L during GA03), likely because of the higher productivity observed in the subpolar compared to the subtropical North Atlantic. On the other hand, both cruises have similar order of magnitudes in the whole water column for pCd (up to 7.1 and 1.5 pmol/L for GEOVIDE and GA03, respectively), pCo (up to 1.5 and 8.3 pmol/L for

GEOVIDE and GA03, respectively), pCu (up to 36 and 28 pmol/L for GEOVIDE and GA03, respectively), pNi (up to 70 and 158 pmol/L for GEOVIDE and GA03, respectively) pV (up to 92 and 87 pmol/L for GEOVIDE and GA03, respectively) and pZn (up to 0.9 and 0.3 nmol/L for GEOVIDE and GA03, respectively). However, concentrations during GEOVIDE of pAl (0.1-15 nmol/L), pFe (0.02-3.2 nmol/L) and pTi (0.004-0.2 nmol/L) are lower than those observed during GA03 (0.1-98, 0.04-25 and 0.004-3.6 nmol/L, respectively [44]). This might be due to the fact that both cruises took place at different latitudes, with the GA03 transect located in the dust rich region of the Atlantic.

3.2. Particulate TE:^{234}Th and mineral:^{234}Th ratios in the large size fraction (>53µm)

Magnitudes of ratios differ among elements (pCd:^{234}Th, pCo:^{234}Th < pCu:^{234}Th, pNi:^{234}Th, pV:^{234}Th < pMn:^{234}Th, pTi:^{234}Th, pZn:^{234}Th < pFe:^{234}Th < pAl:^{234}Th, pP:^{234}Th) and vary between basins as described below. Profiles of pTE:^{234}Th and mineral:^{234}Th ratios in the >53 µm fraction generally follow those observed for the concentrations (Fig. S4).

Ratios of pAl:^{234}Th (1204 nmol/dpm) or lithogenic:^{234}Th (404 µg/dpm) reach highest values at 250m at Station #1. Similarly, highest pCo:^{234}Th (0.08 nmol/dpm), pCu:^{234}Th (0.4 nmol/dpm), pFe:^{234}Th (245 nmol/dpm), pMn:^{234}Th (4 nmol/dpm) and pTi:^{234}Th (18 nmol/dpm) occur at 250m at Station #1. Lithogenic:^{234}Th ratios generally increase with depth but also show elevated values at the surface (15-30m) of Stations #1, #21 and #32.

High pP:^{234}Th and pV:^{234}Th ratios are observed in the upper 100m of the Irminger and Labrador basins (reaching 121 and 0.9 nmol/dpm, respectively), like high opal:^{234}Th ratios (750 µg/dpm at 30m of Station #69). In the west European and Icelandic basins, ratios of pCd:^{234}Th, pCo:^{234}Th, pCu:^{234}Th, pFe:^{234}Th, pNi:^{234}Th, pP:^{234}Th and pZn:^{234}Th increase towards the surface, similarly to $CaCO_3$:^{234}Th (reaching 271 µg/dpm at 109m at Station #38).

Some exceptions are observed at 60m at Station #64 and in the Icelandic basin, especially at 200m at Station #32, where we determined high ratios of pCo:^{234}Th (0.01 and 0.04 nmol/dpm at Stations #64 and #32, respectively), pCu:^{234}Th (0.17 nmol/dpm at Station #32), pNi:^{234}Th (0.14 and 1.04 nmol/dpm at Stations #64 and #32, respectively) and pZn:^{234}Th (from 1.5 to 5.2 nmol/dpm in the upper 60m of the Icelandic basin). These high values correspond to the highest $Fe(OH)_3$:^{234}Th ratios (6.5 µg/dpm at 60m at Station #64, and 1.04-2.25 µg/dpm in the upper 200m at Station #32). The highest MnO_2:^{234}Th ratios are also observed at 60m at Station #64, and at 153m at Station #26, coinciding with a slight increase of the pZn:^{234}Th ratio (1.2 nmol/dpm).

3.3. Export fluxes

Export fluxes at Eq (between 40 and 110m) significantly vary between elements and between basins (Table 3, Fig. 2). The most striking results are the maximal flux of pAl or lithogenic material (9207 µg/m^2/d and 115 mg/m^2/d, respectively) and of some pTEs in vicinity of the Iberian margin (Station #1), with extreme values for pCo, pFe, pMn, pP and pTi (3.6, 3912, 55, 8141 and 340 µg/m^2/d, respectively). Such high fluxes evidence particulate inputs from the Iberian margin, leading to the export of pTE out of the surface layer.

The highest $CaCO_3$ export fluxes occur within the west European and Icelandic basins, where blooms of coccolithophorids were observed during GEOVIDE [62]. There, we also observe high fluxes of pCd, pCu, pNi or pP, which at Station #21 reach values of 11, 18, 84 and 4648 µg/m^2/d, respectively. Opal fluxes are the highest in the Irminger and Labrador basins, where diatom blooms were declining during GEOVIDE [60] (568 mg/m^2/d at Station #64). Surprisingly, the settling of diatoms in these basins is characterized by low pTE export fluxes.

High $Fe(OH)_3$ export flux is observed in the Icelandic basin (Station 32) and in the western Labrador basin (Station #64). At Station #32, the high $Fe(OH)_3$ flux (1.3 mg/m^2/d) goes with

high fluxes of pAl, pCd, pCo, pCu, pFe, pMn, pNi, pP, pV and pZn (469, 5.1, 2.7, 10, 931, 13, 33, 4145, 1.7 and 396 µg/m^2/d, respectively). Export fluxes of MnO_2 are small compared to other mineral fluxes (0.007 mg/m^2/d compared to 0.36 mg/m^2/d for $Fe(OH)_3$ on average). In general, high fluxes of MnO_2 and $Fe(OH)_3$ coincide but MnO_2 fluxes are particularly high in the west European (Station #26) and Irminger (Station #44) basins where we can observe a slight increase of pCo, pMn and pV fluxes (reaching 0.4, 9.3 and 0.4 µg/m^2/d, respectively, at Station #26).

Particulate TE export fluxes determined using the ^{234}Th approach are still scarce in the literature. Comparing different biogeochemical areas is difficult because of differences in sampling periods (and different productivities), export depths (surface versus deep or Eq depth versus fixed depth) or locations (shelf versus open-ocean). However, the overall ranges of pTE export fluxes between GEOVIDE and the literature are comparable. The pFe export flux at proximity of the Iberian margin (3912 µg/m^2/d) is by far the highest observed along the GEOVIDE transect but is still lower than fluxes determined on the Scotian shelf (7874 µg/m^2/d [88]), or close to the Crozet island (8098 µg/m^2/d [32]), where lithogenic inputs are even higher. Conversely, the lower pAl export fluxes in the Labrador Sea (67-281 µg/m^2/d at GEOVIDE Stations #64, #69 and #77 and 432-594 µg/m^2/d in 2005 [34]) indicate lower lithogenic inputs, which seem to drive lower pFe export fluxes (41-501 µg/m^2/d at GEOVIDE Stations #64, #69 and #77 and 480-614 µg/m^2/d in 2005 [34]). Even though GEOVIDE took place during the spring bloom, export of pP (266-8141 µg/m^2/d) is lower than observed along the GP16 transect, from the Peruvian shelf to the subtropical Pacific gyre (254-27876 µg/m^2/d [36]) likely due to high productivities and high biogenic exports induced by the coastal upwelling there. Similarly, particulate organic carbon (POC) export reaches 960 mg/m^2/d during GP16 compared to 139 mg/m^2/d during GEOVIDE [83]. For that same Pacific ocean area, Black et al. (2019)[36] reports similar pCo fluxes (0.1-4 µg/m^2/d) but much higher pCd (0.2-112 µg/m^2/d) and pMn export

fluxes (6-549 µg/m^2/d) compared to fluxes in the North Atlantic reaching up to 4 µg pCo/m^2/d, 11 µg pCd/m^2/d, 55 µg pMn/m^2/d for the present GEOVIDE section and 3 µg pCd/m^2/d for the Scotian shelf area [88]. Finally, Smith et al. (2014) [88] reports similar pCu export fluxes for the Scotian shelf (1-22 µg/m^2/d) compared to those observed for the GEOVIDE transect (1-16 µg/m^2/d).

3.4. Residence times

Along the GEOVIDE transect, TE inventories and exports, and consequently residence times, vary considerably (Table 5). Trace element residence times in the surface-Eq depth layer range from 2 to 13297 days: Al (4±0.2 - 106±3 days), Fe (2±0.1 - 147±5 days) < Mn (89±25 - 626±80days), Zn (4±0.4 - 582±18 days) < Co (64±3 - 3427±209 days), Cu (236±11 - 3646±698 days) < Ni (339±15 - 13297±407 days).

High particulate and dissolved inventories, high export fluxes and short τ_{total} are observed at Station #1, close to the Iberian margin, for all TEs. There, we observe the shortest residence times for Al (τ_{total}=4 days), Co (τ_{total}=64 days), Cu (τ_{total}=236 days) and Fe (τ_{total}=2 days). However, τ_{total} values for Mn, Zn and Ni at Station #1 are not the shortest ones along the transect.

The Icelandic and western European basins are also characterized by short element residence times. For example, the residence time for Fe is only 3 days (at Stations #32 and #38) and Ni and Zn residence times are shorter there (Ni: τ_{total}=339 days at Station #21; Zn: τ_{total}=4 days at Station #32) than near the Iberian margin. A major difference with the Iberian margin is the generally lower surface water particulate and dissolved inventories for most TEs in the Icelandic and west European basins (Table 5).

Finally, τ_{total} for all TEs are much longer, generally of the order of years (5, 9, 7, 36 and 2 years for Co, Cu, Mn, Ni and Zn respectively) within the Labrador and Irminger basins, while they

484 are less than a year or even only a few days, within the west European/Icelandic and Iberian
485 basins. For example, Fe residence times average 47 days within the Labrador and Irminger
486 basins compared to an average of 10 days for the west European/Icelandic basins and 2 days
487 for Station #1 at the Iberian margin. For all TEs, except Co, τ_{total} is maximal at Station #77 in
488 the Labrador Sea. For Co, the maximum τ_{total} is reached at Station #64, also in the Labrador
489 Sea.
490

491 ## 4. DISCUSSION

492 Since particulate ^{234}Th was not analysed on filters dedicated to trace metal analyses in the SSF,
493 element:^{234}Th ratios could only be determined for the LSF, which is assumed to be
494 representative of sinking particles [89]. To our knowledge, this assumption has been used in all
495 studies dedicated to TE export fluxes and using ISP [31,32,34–36]. We are aware though, that small
496 particles may contribute to the TE export.
497

498 ### 4.1. Statistical analyses

499 In order to gain more insight about the vector phases carrying each elemental flux, we examined
500 the Spearman rank correlation coefficients between TE and mineral exports (XLStat software;
501 Table 4). The analysis was conducted on log-transformed export fluxes to ensure that input
502 variables are more normally distributed and to reduce the influence of extreme values. The
503 influence of lithogenic materials on the pTE export fluxes is highlighted by the significant
504 correlations, especially for pCu, pFe and pZn (p-value < 0.05 and $R \geq 0.9$; Table 4). At a lesser
505 extent but still significantly, pCd, pCo, pNi and pTi export fluxes are also correlated to
506 lithogenic fluxes (p-value < 0.05 and $R \geq 0.6$; Table 4). Biogenic (opal and $CaCO_3$) and oxide
507 ($Fe(OH)_3$ and MnO_2) phases do not show any significant correlations with the pTEs, likely due
508 to the significance of lithogenic particles in controlling TE fluxes in the North Atlantic (Table

509 4). In order to disentangle the roles of the biogenic and oxide phases on pTE fluxes, we used a
510 principal component analysis (PCA; XLStat software) considering excess pTE exports (ie. pTE
511 export fluxes corrected from the lithogenic fraction; Fig. 3). Recent studies have applied a PCA
512 approach for large datasets of element concentrations, including small and large particle size
513 fractions [19,44,65,90], but we only consider here export fluxes at the Eq depth based on the large
514 particle size fraction (with GEOVIDE particulate concentrations being reported and discussed
515 elsewhere; Planquette et al., personal communication, 2019 and Gourain et al., 2019 [65]). To
516 only comment on the distribution of the pTEs, neither mineral exports nor chemical variables
517 are included in the PCA. The PCA has been conducted after a Varimax rotation which appeared
518 to clarify the relationship among variables by better capturing known dynamics of the water
519 column [19,91]. This analysis is also conducted on log-transformed export fluxes to limit the
520 influence of extreme values and to ensure a more normal distribution of the variables [19,92]. We
521 identified four principal components that together explain 95% of the total dataset variance
522 (Fig. 3).
523 The first principal component (33 % of the total variance) likely describes the biological
524 influence as it explains 84 and 81% of the excess pCd and pP flux variances, respectively. This
525 component also explains 55% of the excess pCu flux and between 9 and 17% of the excess
526 pCo, pNi and pZn fluxes. In Table 4, pP appears to be correlated with most pTEs (p-value <
527 0.05 and $R > 0.65$ for pCd, pCo, pCu and pMn fluxes and $R > 0.45$ for pAl, pNi and pZn). To
528 investigate the biological influence on pTE fluxes, we also examined their correlations with
529 POC, $CaCO_3$ and opal. No significant correlation was observed.
530 The second component (30% of the total variance) explains 74% of both excess pCo and pZn
531 fluxes variances and also explains, at a lesser extent, the export fluxes of other pTEs (12-41%
532 of excess pCd, pCu, pNi variances and 6% of excess pP variance). Interestingly, Ohnemus et
533 al. (2019) also found a factor strongly driven by pCo abundances, with additional - smaller -

534 contributions for other pTEs. They related this factor to a secondary (heterotrophic) biomass
535 phase [19].
536 The third principal component (19% of the total variance) is strongly indicative of authigenic
537 Fe oxides, as it explains 89% of the variability of excess pFe fluxes. In addition, this third
538 component also explains 21% of the variance of excess pNi flux and between 4 and 9% of the
539 variances of excess pCo, pCu, pMn, pP and pZn fluxes, reflecting the scavenging of these TEs
540 onto this authigenic phase [93]. Furthermore, the correlation analysis highlights links between
541 authigenic Fe oxide and Mn oxide fluxes (R=0.77), $CaCO_3$ fluxes (R=0.63) and pTEs,
542 especially pNi, pCu and pZn fluxes (R = 0.30 – 0.46; Table 4).
543 Finally, the fourth component (14% of the total variance) probably describes the influence of
544 authigenic Mn oxides as it explains 90% of the variance of excess pMn fluxes. It is associated
545 at 6-8% with excess pFe and pNi fluxes, and at 1-3% with pCd, pCo, pCu and pP fluxes.
546
547 4.2. Lithogenic contribution to fluxes
548 Lithogenic particles play a central role in the North Atlantic (Table 4). They can originate from
549 different sources such as atmospheric deposition, glacial meltwater, advection of sediment-
550 enriched water masses or lateral mixing with shallow coastal waters under continental
551 influence. The importance of lithogenic sources is particularly clear for Station #1, suggesting
552 an input from the Iberian margin (Fig. 2) in agreement with the literature [44,59]. There, we
553 determined the highest fluxes for lithogenic material and some pTEs, which were accompanied
554 by pTE:pAl ratios close to UCC [67] (Fig. 4; Fig. S5). This is especially the case for pFe and pMn
555 for which the respective ratios show only 2 and 20% offset relative to UCC ratios (Fig. 4). For
556 other pTEs, these ratios are slightly greater than for UCC, pointing to the presence of another
557 driver of export fluxes. Such TE enrichments relative to the UCC have also been reported in
558 the estuary of the Tagus river [94] for which the plume has been shown to reach Station #1 [69,85].

559 This river is known to receive effluents from agricultural, industrial and urban sources and thus
560 represents an important discharge of dissolved and particulate TE concentrations to the estuary
561 [95–98]. The slightly higher pTE:pAl ratios compared to UCC may indicate that fluxes at Station
562 #1 are under anthropogenic influence via the discharge from the Tagus estuary.
563 Stations at proximity of the Greenland and Newfoundland margins are also characterized by
564 some higher pTE:pAl ratios (i.e., pCd:pAl or pCu:pAl; Fig. 4), implying additional processes
565 in the export of these pTEs. Although lithogenic particles settle quickly through the water
566 column, they can also adsorb elements onto their surfaces [44,99,100]. Such scavenging processes
567 could explain the higher pTE:pAl ratios. Interestingly, the Greenland and Newfoundland
568 margin stations are characterized by much lower lithogenic and pTE flux intensities compared
569 to the Iberian margin (Fig. 2), suggesting that lithogenic material is not similarly released at all
570 margins. Such differences can depend on the morphology of the margin and on the
571 hydrodynamical forcing, providing (or not) significant amounts of lithogenic particles and
572 leading (or not) to the formation of nepheloid layers [101]. Indeed, relatively high lithogenic
573 export fluxes are also observed at open-ocean stations beyond the Iberian margin (up to Station
574 #32). The Iberian margin is known to be an efficient exporter of particulate matter to the open
575 and deep sea [102,103] and during GEOVIDE, high proportions of lithogenic particulate rare earth
576 elements [101] and pFe [65] were observed up to 1700 km far from the Iberian margin. These
577 enrichments were attributed to the presence of intermediate nepheloid layers transported along
578 the isopycnals, which then likely drive pTEs fluxes to the deep ocean. To a lesser extent,
579 lithogenic particles were also transported to the west of the Greenland margin [65], in line with
580 the moderate lithogenic export fluxes observed at Station #64, in the eastern Labrador basin.
581 Conversely, lithogenic particles do not seem to spread off the Newfoundland margin, thereby
582 explaining the lower lithogenic export fluxes at Station #77.
583

584 4.3. Authigenic contribution to fluxes

585 High fluxes of Mn- and Fe-oxides were determined at some stations close to margins, also
586 under lithogenic influence (i.e. Station #64), and at open-ocean stations, which are not
587 necessarily characterized by high particulate lithogenic exports. For example, Station #26
588 presents one of the lowest lithogenic and $Fe(OH)_3$ fluxes, while MnO_2 fluxes are among the
589 highest at this station. This decoupling between high pMn and low pAl fluxes has already been
590 observed and was attributed to a distant shelf source of lithogenic particles [30]. Indeed, nepheloid
591 layers sourced at the shelves lose particles by gravitational settling during lateral advection,
592 but in the case of Mn, it has been shown that dissolved Mn, remobilized from the shelf, oxidizes
593 very slowly, enriching the particulate phase during transport [104]. Long distance transport
594 inducing a subsurface pMn maximum was observed off the Kuril/Kamchatka margin, in the
595 western subarctic Pacific [18]. High pMn concentrations and fluxes at Station #26 could thus have
596 originated from authigenically precipitated Mn during its transport from the American coasts,
597 via the North Atlantic Current (NAC, Fig. 1). The distance between Station #26 and North
598 Carolina coasts (USA) is around 4500km, which roughly corresponds to the distance of
599 4220km calculated by multiplying a NAC velocity of 0.4 m/s [105] by the inverse of the oxidation
600 rate constant of Mn ($k_{ox}=0.341\times10^{-3}$ h^{-1} [106]). Interestingly, the high Mn-oxide fluxes determined
601 at Stations #26, #32, #44 and #64 and to a lesser extent at Stations #13 and #38 drive other pTE
602 fluxes. Indeed, Figure 3 shows that Mn oxides could be responsible for 3-8% of the excess
603 export fluxes of pCu, pFe and pNi.

604 Similarly, Fe-oxide fluxes are high at Stations #32, #38 and #64. As seen in Figures 2 and 3,
605 Fe-oxides could represent an important carrier phase for pCo, pCu, pMn, pNi and pZn (from 4
606 to 21% of the variance explained in the PCA on excess - i.e., non-lithogenic - fluxes, as already
607 discussed in other studies [46, 107, 19].

608

609 4.4. Biogenic contribution to fluxes

610 In addition to Figure 3 and Table 4, the comparison of pTE:POC ratios at each station with
611 those of phytoplankton cells suggests that biogenic particles partly influence pTE exports (Fig.
612 5). Despite large uncertainties associated with this approach, some pTE:POC ratios are
613 comparable to ratios reported for functional phytoplankton groups (diatoms, autotrophic
614 flagellates and autotrophic picoplankton) collected in the upper 150m of the North Atlantic [71]
615 (Fig. 5; Fig. S5). This suggests that pTE exports, and especially those of pCd, pCo, pCu, pMn,
616 and pZn, can also be driven by biogenic particles. However, higher pTE:POC ratios than cell
617 ratios are also observed. Trace elements are known to be scavenged onto particles with depth
618 [12,108] (see previous sections) and it is usual to observe an increase of the bulk ratios compared
619 to cellular ratios [24,109,110]. This can be caused by the presence of detrital, authigenic and
620 lithogenic particles on the filters leading to an increase of the pTE:POC, as observed in Figure
621 5. Moreover, the intracellular TE:C considerably changes between taxa and regions depending
622 on the environmental conditions (e.g. nutrients, sunlight limitations [3]): Fe:C quota usually
623 range between 10-1700 µg/g for diatoms and coccolithophorids in natural and culture
624 experiments [3,111,112] but Sunda and Huntsman (1995) have measured a Fe:C ratio equalling
625 8230 µg/g [113], highlighting the high variability of the ratio and the difficulty to generalize the
626 intracellular phytoplankton TE:C ratios. Therefore, we searched for indicators of the
627 phytoplankton community structure, such as $CaCO_3$, opal and pigment analyses using
628 CHEMTAX [62]. The highest $CaCO_3$ fluxes have been determined within the west European and
629 Icelandic basins (Fig. 2) where coccolithophorids were present [62]. The contribution of
630 coccolithophorids to export pZn, pCu, pNi and pMn is indicated by relatively high correlation
631 coefficients ($0.3<R<0.5$) between these pTEs and $CaCO_3$ exports (Table 4). Opal fluxes are
632 high at Stations #51, #64 and #69 (Irminger and Labrador basins; Fig. 2) where diatoms
633 dominate the phytoplankton community [62]. In the Labrador Sea, high POC and opal fluxes are

associated with surprisingly low pTE export fluxes (Fig. 2). This basin was sampled during the decline of the bloom (Station #69: 7 weeks after the bloom peak) and was also characterized by an important remineralization event in the mesopelagic layer, evidenced from the excess barium (Ba_{xs}) proxy [114]. Both results suggest either a pTE accumulation in surface waters while POC would be preferentially exported, or a limitation of dissolved TEs that would impede a pTE export due to enhanced recycling in surface waters [115].

4.5. Residence time of TEs and efficiency of export

Although only few TE residence times within the upper ocean are available in the literature, the τ_{total} values estimated from the present dataset are comparable with those of other studies. In the surface global ocean, the majority of τ_{total} for Fe fall between 10 and 100 days [35], which corresponds to the 2-147 days range estimated in this study. Hayes et al. (2018) examined the dissolved TE residence times in the upper 1000m of the North Atlantic (note the wider depth layer) and found that Fe had the shortest residence time relative to other TEs, of about 30-60 days [25]. The authors estimated dissolved residence times of less than 6 years for Zn, Co and Mn (0.01 to 6 years in our study, except at Station #64 where τ_{total} for Co reaches 14 years) and of 80-90 years for Cu (0.65-15 years in this study; Table 5). The good consistency between these different studies allows us to rank the turnover rate of TEs in the upper ocean as follows: Fe < Zn < Mn < Co < Cu.

In the following, our attention is mainly devoted to Fe (Fig. 6). The shortest τ_{total} (2 days) is observed close to the Iberian margin, indicating an efficient Fe export. Similar short τ_{total} within the upper ocean (<5 days) have been observed in coastal areas where lithogenic particles probably play an important role in transporting TEs out of the upper ocean [32,35,88]. These lithogenic particles advected from margins may represent a continuous Fe input in surface waters explaining the high inventories and export observed during GEOVIDE at Station #1,

659 even in post-bloom conditions. For example, they contribute for 98% of the total Fe export at
660 Station #1 (Fig. 6). As it consists of dense particles, the sinking rate of lithogenic material is
661 known to be high. Here the particle sinking rate is estimated by dividing the particulate
662 residence time by the surface-Eq depth layer. At Station 1, the sinking rate reaches 63 m/d for
663 pFe, which is in the same order of magnitude as estimated using Stokes law (88 m/d for a
664 particle of 53µm diameter and of density of 1860 kg/m^3, representing an average density for a
665 mixed aggregate composed of lithogenic, transparent exopolymer particles (TEP), detritus,
666 opal and $CaCO_3$; [116]). Similarly, high particulate and dissolved inventories, high export fluxes
667 and short τ_{total} are observed at Station #1 for other TEs, suggesting a fast supply to and removal
668 from the upper ocean by lithogenic particles (Table 5). However, τ_{total} values for Mn, Zn and
669 Ni at Station #1 are not the shortest observed along the transect, indicating that lithogenic
670 particles are not the only drivers of TE export, even at this coastal station.
671 The Icelandic and western European basins were sampled during the bloom development and
672 were thus characterized by an important productivity event [60,61]. In these basins, we observe a
673 τ_{total} averaging 3 days for Fe, suggesting an efficient transport to the deep ocean. As seen
674 previously, Stations #21, #32 and #38 are characterized by high export fluxes of Fe- and Mn-
675 oxides, carrying other TEs to the deep ocean. At these stations, pFe sinks faster compared to
676 the Iberian margin (up to 135 m/d at Station #32), likely because of the presence of Fe-oxides
677 (contributing to 62% of total Fe export in these basins; Fig. 6). These mineral phases are
678 presumably denser than lithogenic particles (the density of ferrihydrite is about 3.8 g/cm^3
679 compared to a typical clay density of 2.7 g/cm^3) but the sinking speed is also controlled by the
680 size of the particle, which might be an important factor in the west European and Icelandic
681 basins. Other TEs also have short τ_{total} and high sinking rates in these basins, confirming the
682 important contribution of oxides to export pTEs.

683 Finally, the Labrador and Irminger basins were sampled during the bloom decline and the
684 average pFe export flux is the lowest of the whole transect (182 µg/m^2/d compared to 441 and
685 3912 µg/m^2/d for respectively the west European/Icelandic basins and Iberian margin). Longer
686 residence times are also determined within the Labrador and Irminger basins, suggesting that
687 most of pFe is not exported as efficiently as in the eastern basins. This may be due to the more
688 important fraction of Fe carried by biogenic matter (12% compared to 1 and 3% in the Iberian
689 and west European/Icelandic basins, respectively), leading to a slower export of Fe and/or
690 active recycling processes. The median sinking rate of 3 m/d (Table 5) is similar to the rate
691 estimated by using Stokes law (3.5 m/d) for an organic particle of 53µm diameter and a density
692 of 1060 kg/m^3. Indeed, Fe removal rate from the upper ocean via biological processes has been
693 shown to be much smaller than via lithogenic and authigenic processes [35]. A greater τ_{total} is also
694 estimated for other TEs. The slower removal of biogenic TEs can also be reflected by the longer
695 residence times of less detrital TEs, such as Ni, Co or Cu (from 65 days to >35 years) compared
696 to more detrital TEs (Al, Fe with τ_{total} <150 days).
697

698 **CONCLUSION**

699 Using the ^{234}Th approach and the elemental composition of large, sinking particles, this study
700 investigated the pTE export fluxes, sinking rates and residence times in the North Atlantic.
701 Lithogenic material is present everywhere along the section, but mainly controls the fluxes near
702 the Iberian margin, where the highest pTE fluxes are observed. As a result, TE residence time
703 in the upper ocean is short in vicinity of the Iberian Margin. In the open ocean, and especially
704 within the Icelandic basin, Mn- and Fe-oxides are likely the main TE carriers to the deep ocean.
705 Zinc and Ni, for example, have shorter residence times there compared to the Iberian basin
706 which is under lithogenic influence. Biogenic particles also contribute to export pTEs, as
707 reflected by the similarity of pTE:POC export ratios and TE:C cell ratios. Particulate TE export

fluxes especially those of pZn, pCu, pNi and pMn might be enhanced by sinking coccolithophorid cells within the west European and Icelandic basins, where $CaCO_3$ exports are the highest. Diatoms are dominating the phytoplankton community within the Irminger and Labrador basins, in agreement with the highest opal fluxes. However there, pTE fluxes are low, possibly suggesting TE recycling due to dissolved TE limitations in surface waters, in line with the decline of the bloom. The inefficient pTE export in this area is also illustrated by the longer residence times, which may be due to greater biogenic contribution.

715

FIGURE 1

a)

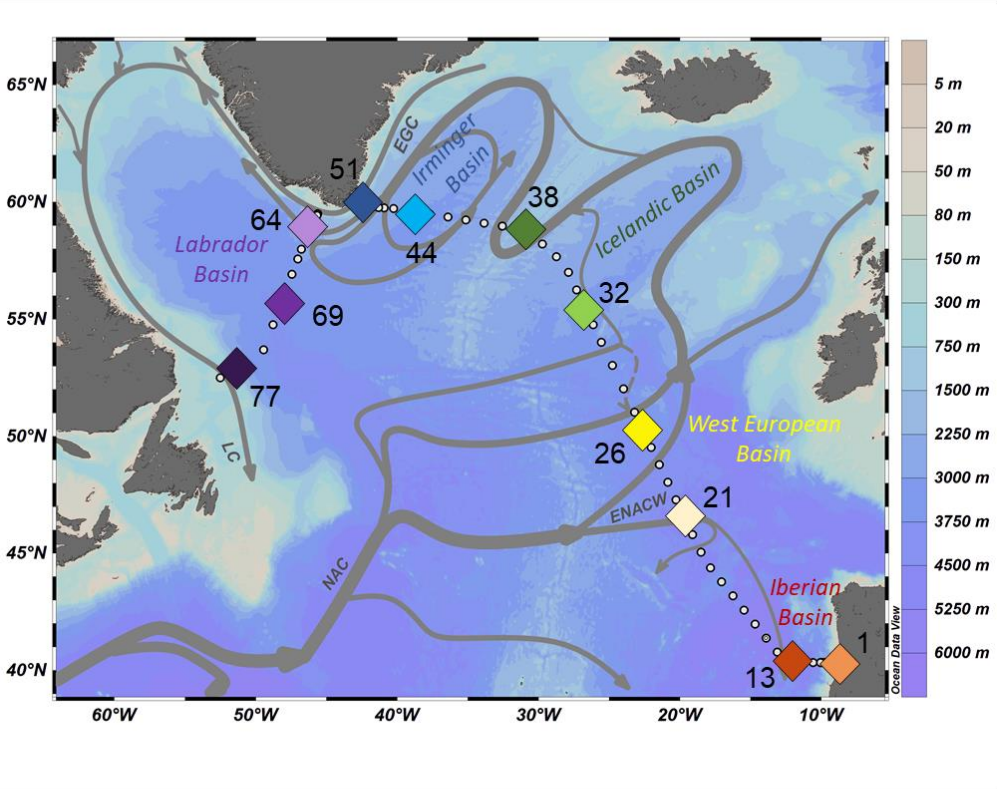

b)

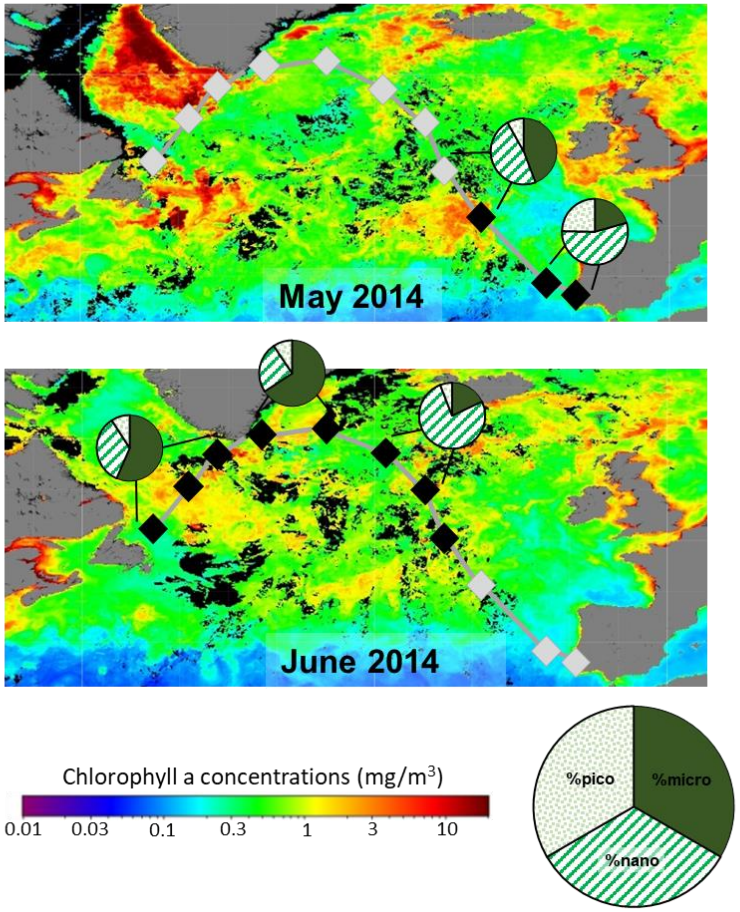

716

Figure 1: a) Schematic diagram of the surface circulation superimposed on the bathymetric map of the North Atlantic [117]. Coloured symbols represent the stations discussed in this study (red: Iberian basin; yellow: West European basin; green: Icelandic basin; blue: Irminger basin; purple: Labrador basin). Abbreviations for the main surface hydrographic features in the upper 500m indicate the East North Atlantic Central Water (ENACW), Labrador Current (LC), East Greenland Current (EGC) and the North Atlantic Current (NAC). b) Satellite-derived chlorophyll-*a* concentrations (MODIS Aqua from oceancolor.gsfc.nasa.gov) averaged over May (top panel) and June (bottom panel) 2014. The GEOVIDE transect is indicated by the grey line and black symbols indicate stations sampled during the corresponding month. The pie charts indicate the proportion of micro-phytoplankton (dark green), nano-phytoplankton (hatched green) and pico-phytoplankton (dotted light green) encountered in each basin during GEOVIDE [62].

FIGURE 2

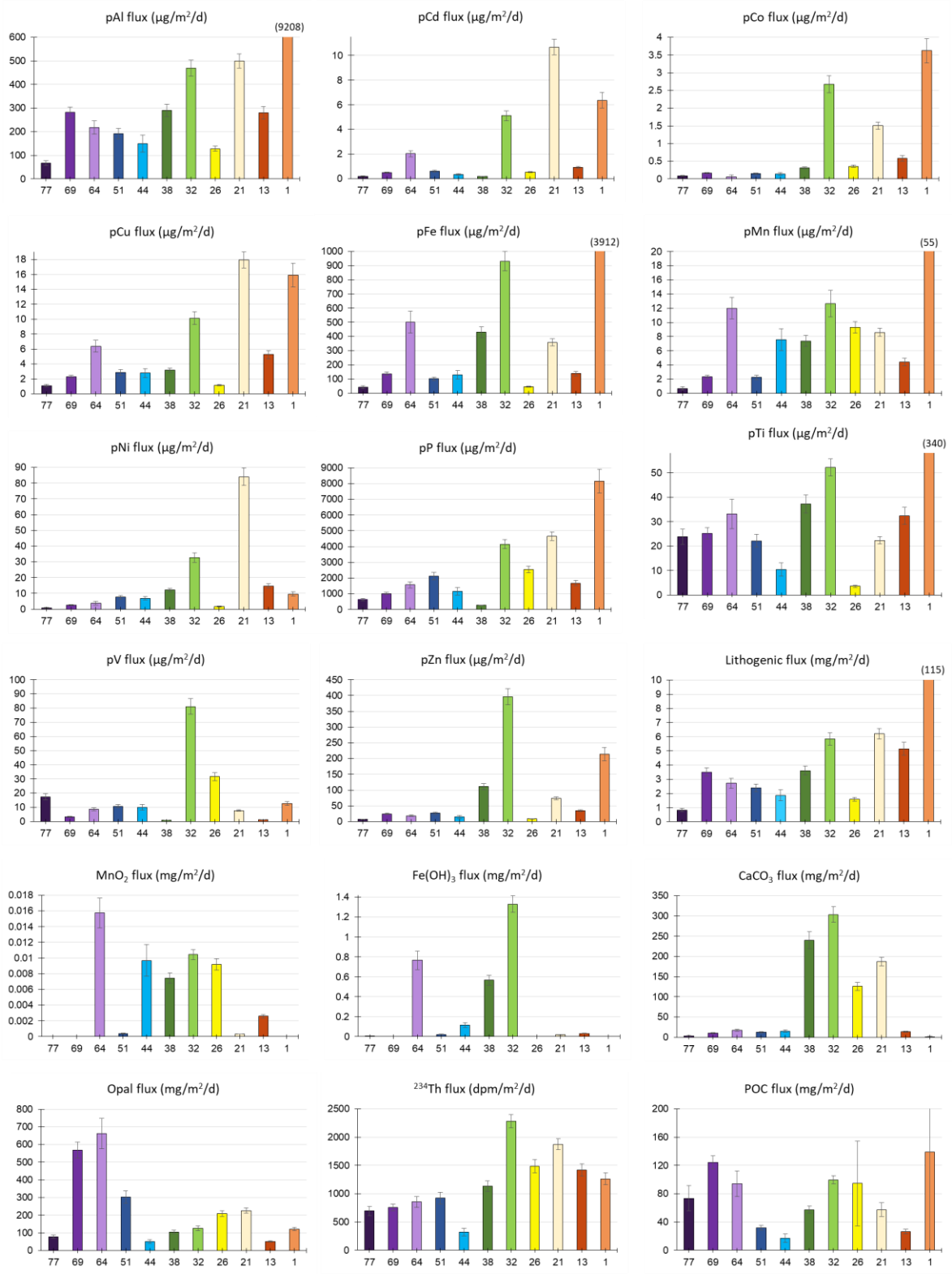

Figure 2: Particulate trace element and mineral export fluxes in µg/m^2/d or mg/m^2/d estimated in the large size fraction at the Eq depth. ^{234}Th (in dpm/m^2/d) and POC (in mg/m^2/d) export fluxes in the large size fraction and at the Eq depth are also presented for comparison [60].

FIGURE 3

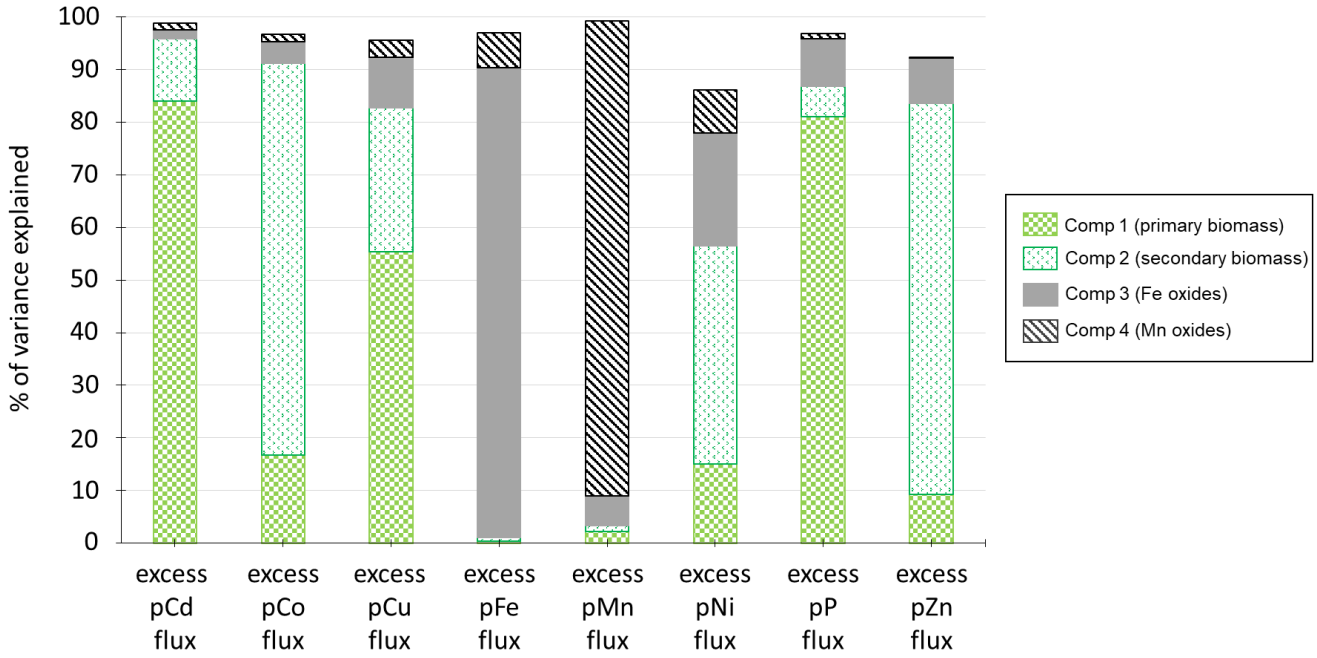

Figure 3: Variance explained for eight excess pTE export fluxes at Eq, captured by the first four principal components in principal component analysis (XLStat software). The description of the components is provided in the text. Excess pTE export fluxes are calculated by removing the lithogenic fraction of the flux (excess pTE flux = pTE flux – [pAl flux × $(\frac{pTE}{pAl})_{UCC}$]; with the UCC ratio from [67]).

FIGURE 4

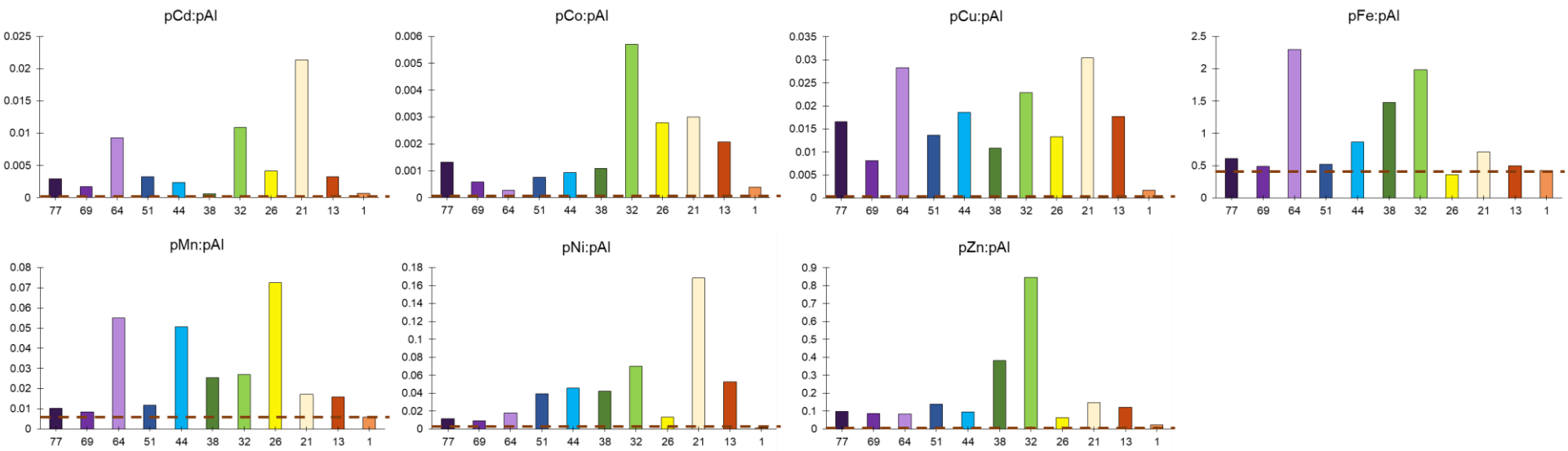

Figure 4: Ratios of the pTEs over pAl fluxes (in g/g, on y-axis) determined at Eq along the GEOVIDE transect (station numbers on x-axis). The brown horizontal dashed lines represent the ratios for the upper continental crust (UCC) [67].

FIGURE 5

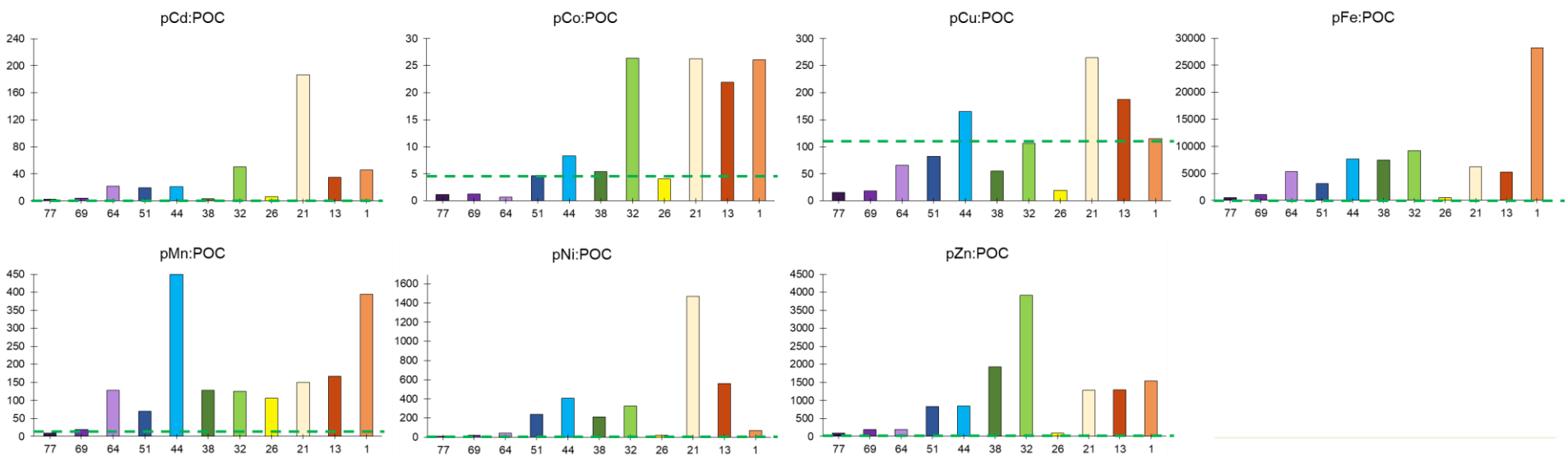

Figure 5: Ratios of the pTEs over particulate organic carbon (POC) fluxes (in µg/g, on y-axis) determined at Eq along the GEOVIDE transect (station numbers on x-axis). The green horizontal dashed lines indicate the average intracellular metal stoichiometries [71].

FIGURE 6

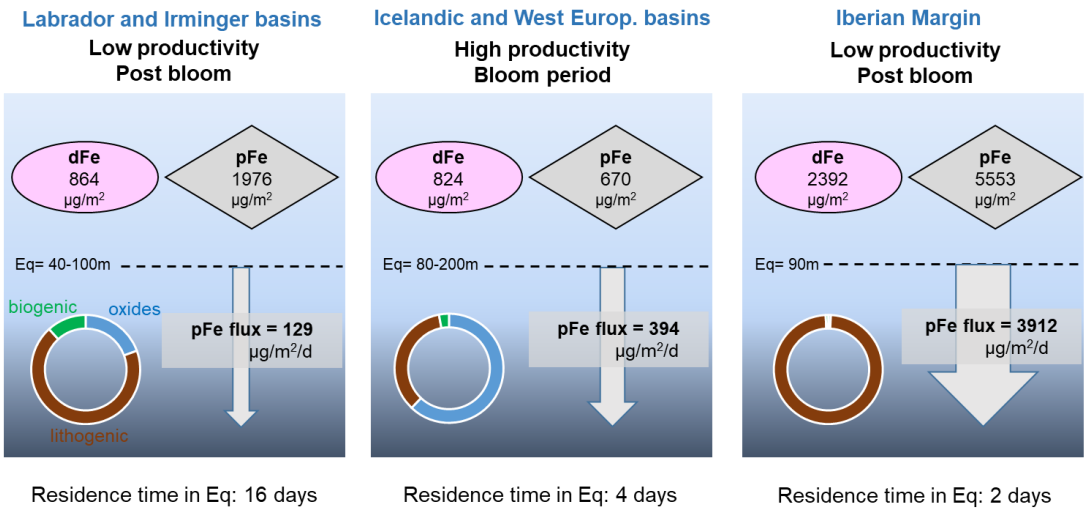

Figure 6: Biogeochemical iron budget in the upper ocean for the Labrador and Irminger basins (left box), for the Icelandic and west European basins (middle box) and for the Iberian margin (right box). For each area, we show the median inventories of dissolved iron (dFe [85]; pink circles) and particulate iron (pFe [65]; grey diamonds) in µg/m^2, the median particulate iron fluxes (pFe flux; grey rectangles) in µg/m^2/d and the median total residence times (τ_{tot}) in days. The total residence time is calculated for the depth interval 0-Eq. The size of the arrows is roughly proportional to the magnitude of the pFe fluxes. The fractions of the pFe flux driven by lithogenic, authigenic or biogenic particles are represented by the brown, blue and green colours, respectively. Lithogenic pFe flux was estimated by multiplying the pAl flux by the pFe:pAl ratio in the upper continental crust (UCC, i.e., 0.44 g/g) [67]. Authigenic pFe flux is equal to the $Fe(OH)_3$ flux (see details in section 2.3) and the biogenic pFe flux is obtained by multiplying the POC flux [60] by an average Fe:C ratio determined in phytoplankton cells of the North Atlantic (193.7 µg/g) [71].

TABLE 1

	Station	Number of weeks since beginning of spring bloom	In-situ primary production (mmol/m^2/d)	Phytoplankton class	POC export (mmol/m^2/d)
Iberian basin	1	10	33	diatoms & coccolith.	12
	13	11	79	pelagophytes & cyano.	2.2
west Europ. Basin	21	9	135	diatoms	4.8
	26	8	174	diatoms	7.9
Icelandic basin	32	5	105	coccolith.	8.3
	38	4	68	coccolith.	4.8
Irminger basin	44	5	137	diatoms	1.4
	51	4	166	diatoms	2.7
Labrador basin	64	5	54	diatoms	7.8
	69	4	27	diatoms	10
	77	5	80	diatoms	6.1

Table 1: Station characteristics with the number of weeks between the sampling time and beginning of the spring bloom (obtained from satellite data products [60]), primary production (obtained from incubations [61]), POC export fluxes (obtained with the ^{234}Th approach [60]), and phytoplankton classes (from HPLC pigment analysis and CHEMTAX analysis [62]).

TABLE 2

	Al^{+}	Ca^{+}	Cd	Co*	Cu	Fe*	Mn	Na$^{\wedge}$	Ni	P^{+}	Ti^{+}	V	Zn
Blank (ppm)	1.6E-03	1.4	1.2E-06	3.2E-06	1.3E-05	1.5E-03	1.4E-04	936	3.4E-04	2.5E-03	1.0E-04	7.3E-06	2.6E-04
BCR-414 (n=5; ppm)	3112	51133	0.385	1.44	29.7	1860	301	6601	17.8	15541	95	9	112.4
RSD (%)	15	2.1	5.2	15	13	12	14	0.2	16	24	8	1	17
Recovery CRM (%)	118	80	101	101	101	101	101	/	95	113	75	111	101

Table 2: Blanks, average concentrations of the certified reference material (CRM; BCR-414), relative standard deviation (RSD) of the 5 analyses of the CRM and recoveries. Elements without any superscript sign have certified concentrations (Cd, Cu, Mn, Ni, V and Zn); elements marked with (*) have indicative concentrations reported on the official certificate (Co and Fe); elements marked with ($^{+}$) have indicative concentrations reported on the GEOREM website (Al, Ca, P, and Ti) and Na has no reported concentration. The official certificate can be found at https://crm.jrc.ec.europa.eu/p/40455/40461/By-material-matrix/Animal-materials/BCR-414-PLANKTON-trace-elements/BCR-414 .

TABLE 3

Basin	Station	Eq	Al flux		Cd flux		Co flux		Cu flux		Fe flux		Mn flux		Ni flux		P flux		Ti flux		V flux		Zn flux	
		m	µg/m^2/d	sd	µg/m^2/d	sd	µg/m^2/d	sd	µg/m^2/d	sd	µg/m^2/d	sd	µg/m^2/d	sd	µg/m^2/d	sd	µg/m^2/d	sd	µg/m^2/d	sd	µg/m^2/d	sd	µg/m^2/d	sd
Iberian	1	90	9208	883	6.4	0.6	3.6	0.3	16	2	3912	364	55	6	9.7	1.4	8141	758	340	34	13	1	214	21
	13	110	280	26	0.9	0.1	0.58	0.08	5.0	0.5	138	15	4.4	0.5	15	1	1673	160	32	4	1.2	0.1	34	3
west Europ.	21	110	500	30	10.7	0.6	1.5	0.1	15	1	358	25	8.6	0.6	84	6	4648	278	22	1	7.8	0.5	74	5
	26	100	128	11	0.53	0.05	0.36	0.03	1.7	0.1	46	4	9.3	0.8	1.7	0.2	2537	212	3.5	0.4	32	3	8	1
Icelandic	32	130	469	35	5.1	0.4	2.7	0.2	11	1	931	69	13	2	33	3	4145	285	52	4	81	5	396	25
	38	80	290	26	0.18	0.02	0.31	0.03	3.1	0.3	429	40	7.4	0.8	12	1	266	24	37	4	1.0	0.1	111	10
Irminger	44	40	150	36	0.36	0.07	0.14	0.04	2.8	0.6	129	30	7.6	1.6	6.9	1.1	1158	237	10	3	10	2	14	6
	51	100	192	22	0.63	0.07	0.15	0.02	2.6	0.3	101	12	2.2	0.3	7.6	1.0	2105	242	22	3	11	1	26	3
Labrador	64	80	218	29	2.0	0.2	0.06	0.05	6.2	0.8	501	77	12	2	3.8	1.2	1562	185	33	6	8.6	1.0	18	2
	69	40	281	23	0.49	0.04	0.16	0.01	2.3	0.2	137	11	2.4	0.2	2.6	0.3	1017	82	25	2	3.2	0.3	24	2
	77	60	67	10	0.19	0.02	0.09	0.01	1.1	0.1	41	10	0.7	0.2	0.8	0.3	627	73	24	3	17	2	7	1

Basin	Station	Eq	Lithogenic flux		$Fe(OH)_3$ flux		MnO_2 flux		$CaCO_3$ flux		Opal flux		^{234}Th flux	
		m	mg/m^2/d	sd	mg/m^2/d	sd	mg/m^2/d	sd	mg/m^2/d	sd	mg/m^2/d	sd	dpm/m^2/d	sd
Iberian	1	90	115	11	nd	nd	nd	nd	nd	nd	122	10	1264	104
	13	110	3.5	0.3	0.032	0.003	0.0026	0.0002	14	1	52	4	1418	111
west Europ.	21	110	6.2	0.4	0.020	0.001	0.00032	0.00002	187	10	226	14	1873	97
	26	100	1.6	0.1	nd	nd	0.009	0.001	126	10	209	17	1486	117
Icelandic	32	130	5.8	0.4	1.3	0.1	0.010	0.001	303	19	127	13	2282	119
	38	80	3.6	0.3	0.57	0.05	0.007	0.001	240	21	105	9	1134	95
Irminger	44	40	1.9	0.4	0.11	0.02	0.010	0.002	15	3	51	11	321	66
	51	100	2.4	0.3	0.024	0.003	0.00038	0.00004	12	1	303	34	922	103
Labrador	64	80	2.7	0.4	0.8	0.1	0.016	0.002	17	2	661	86	855	95
	69	40	3.5	0.3	nd	nd	nd	nd	10	1	568	46	758	57
	77	60	0.8	0.1	0.0	0.0	nd	nd	3	1	79	9	696	77

Table 3: Particulate export fluxes in µg/m^2/d for aluminum (pAl), cadmium (pCd), cobalt (pCo), copper (pCu), iron (pFe), manganese (pMn), nickel (pNi), phosphorus (pP), titanium (pTi), vanadium (pV) and zinc (pZn); in mg/m^2/d for lithogenic material, iron oxides ($Fe(OH)_3$), manganese oxides (MnO_2), calcium carbonate ($CaCO_3$), opal and in dpm/m^2/d for ^{234}Th. Standard deviations (sd) were calculated by considering the standard deviations of the ^{234}Th fluxes and pTE:^{234}Th ratios at Eq, with all concentration and activity uncertainties estimated using error propagation law.

TABLE 4

Variables	Lithogenic flux	$Fe(OH)_3$ flux	MnO_2 flux	$CaCO_3$ flux	Opal flux	POC flux	Al flux	Cd flux	Co flux	Cu flux	Fe flux	Mn flux	Ni flux	P flux	Ti flux	V flux	Zn flux
Lithogenic flux	**1**																
$Fe(OH)_3$ flux	0.083	**1**															
MnO_2 flux		**0.769**	**1**														
$CaCO_3$ flux	0.200	**0.633**	**0.706**	**1**													
Opal flux	0.164		0.028	0.073	**1**												
POC flux	0.391				0.473	**1**											
Al flux	**1.000**	0.083		0.200	0.164	0.391	**1**										
Cd flux	**0.618**	0.018	0.037	0.100	0.364	0.273	**0.618**	**1**									
Co flux	**0.745**			0.200		0.282	**0.745**	0.591	**1**								
Cu flux	**0.845**	0.330	0.156	0.255	0.064	0.191	**0.845**	**0.791**	**0.609**	**1**							
Fe flux	**0.855**	0.395	0.220	0.273	0.145	0.455	**0.855**	0.591	0.527	**0.900**	**1**						
Mn flux	0.527	0.183	0.440	0.364	0.136	0.473	0.527	**0.636**	0.527	**0.718**	**0.736**	**1**					
Ni flux	**0.764**	0.440	0.138	0.491			**0.764**	0.573	**0.673**	**0.791**	**0.636**	0.345	**1**				
P flux	0.491			0.073	0.209	0.236	0.491	**0.891**	**0.718**	**0.627**	0.400	**0.655**	0.473	**1**			
Ti flux	**0.691**	0.312		0.018	0.000	0.564	**0.691**	0.300	0.400	**0.627**	**0.845**	0.427	0.409	0.100	**1**		
V flux			0.119		0.009	0.336		0.200	0.127			0.327		0.445		**1**	
Zn flux	**0.909**	0.303	0.000	0.318	0.018	0.245	**0.909**	0.527	**0.764**	**0.791**	**0.818**	0.464	**0.855**	0.464	**0.718**		**1**

Table 4: Spearman rank correlation coefficients between trace element and mineral export fluxes for the large size fraction at the Eq depth. The analysis was conducted on log-transformed export fluxes to ensure that input variables were more normally distributed and to reduce the influence of extreme values. Correlations with $R < 0.1$ are not shown. Values in bold are correlation coefficients with p-value ≤ 0.05 (t-test; XLStat software).

TABLE 5

Basin	Station	Al					Co					Cu					Fe				
		diss. invent.	part. invent.	sinking rate	τ_{tot}		diss. invent.	part. invent.	sinking rate	τ_{tot}		diss. invent.	part. invent.	sinking rate	τ_{tot}		diss. invent.	part. invent.	sinking rate	τ_{tot}	
		$\mu g/m^2$	$\mu g/m^2$	m/d	d	sd	$\mu g/m^2$	$\mu g/m^2$	m/d	d	sd	$\mu g/m^2$	$\mu g/m^2$	m/d	d	sd	$\mu g/m^2$	$\mu g/m^2$	m/d	d	sd
Iberian	1	20847	12741	65	4	0.2	219	13	25	64	3	3718	28	52	236	11	2392	5553	63	2	0.1
	13	7720	6672	5	51	5	124	32	2	269	29	5002	129	4	1033	110	1564	1139	13	20	2
west	21	13038	3628	15	33	1	151	37	5	125	5	6224	186	9	422	19	861	599	66	4	0.2
Europ.	26	6181	1741	7	62	12	195	20	2	598	114	6100	133	1	3646	698	691	741	6	31	6
Icelandic	32	12630	1465	42	30	4	224	22	16	92	11	5539	202	7	534	66	1471	898	135	3	0.3
	38	6007	716	32	23	1	111	9	3	380	19	2859	113	2	944	47	786	539	64	3	0.2
Irminger	44	443	1831	3	15	4	49	7	1	401	111	1281	147	1	512	142	809	996	5	14	4
	51	9983	4558	4	76	5	312	2	7	2125	145	8128	200	1	3191	218	1983	3275	3	52	4
Labrador	64	3525	3049	6	30	2	203	4	1	3427	209	5812	160	3	966	59	2086	1976	20	8	0.5
	69	969	3314	3	15	11	31	9	1	245	175	2150	129	1	996	713	294	1915	3	16	12
	77	2621	4465	1	106	3	122	44	0.1	1873	57	3588	237	0.3	3442	105	864	5128	0.5	147	5

Basin	Station	Mn					Ni					Zn				
		diss. invent.	part. invent.	sinking rate	τ_{tot}		diss. invent.	part. invent.	sinking rate	τ_{tot}		diss. invent.	part. invent.	sinking rate	τ_{tot}	
		$\mu g/m^2$	$\mu g/m^2$	m/d	d	sd	$\mu g/m^2$	$\mu g/m^2$	m/d	d	sd	$\mu g/m^2$	$\mu g/m^2$	m/d	d	sd
Iberian	1	6726	408	12	130	6	8236	23	37	854	39	5769	1174	16	32	1
	13	2606	332	1	664	70	11488	167	10	789	84	1355	951	4	67	7
west	21	2134	272	3	280	12	27694	816	11	339	15	2736	536	15	44	2
Europ.	26	2868	204	5	330	63	20682	194	1	12374	2369	1647	552	1	271	52
Icelandic	32	2505	175	9	212	26	19375	193	22	597	74	709	679	76	4	0.4
	38	1018	98	6	151	8	8152	88	11	674	33	790	400	22	11	0.1
Irminger	44	361	312	1	89	25	3611	118	2	544	151	658	757	1	99	27
	51	2317	102	2	1080	74	9212	181	4	1240	85	3668	855	3	171	12
Labrador	64	1833	113	8	162	3	15196	97	3	3987	243	4112	536	3	256	16
	69	152	152	1	129	92	4705	202	1	1902	1361	464	345	3	33	24
	77	1353	461	0.1	2626	80	9488	1006	0.05	13297	407	3177	638	1	582	18

Table 5: Dissolved inventories (diss. invent. from [69,85] and from Planquette et al., personal communication, 2019), particulate inventories (part. invent. from [65] and from Planquette et al., personal communication, 2019), sinking rates calculated as the inverse of particle residence time multiplied by the Eq depth layer; total residence time (τ_{tot}, in days) calculated by dividing the total inventory (dissolved+particulate) by the

particulate flux and its standard deviation (sd) obtained by calculating τ_{tot} at Eq, Eq+20m or Eq-20m (20m being the average error on the determination of the Eq depth).

ASSOCIATED CONTENT

Supporting Information

Figure S1: Summary of the different sampling and analytical steps for the >53µm particle size fraction, collected on in-situ pump (ISP) filters and for total ^{234}Th activities, collected via standard CTD rosette. In this figure, each filter is defined by a nominal porosity (in µm) and a diameter (corresponding to the symbol Ø, in mm).

Figure S2: Mineral fluxes calculated either by using Al (top panel) or Ti (bottom panel) as lithogenic tracers (in mg/m^2/d).

Figure S3: Vertical concentration profiles in the upper 400m (see Table S1 for deeper concentrations) of pTEs and minerals for the >53µm size fraction along the GEOVIDE transect. There are three plots per element: Station #1 (shown alone because of the extreme values observed for few elements); Iberian, west European and Icelandic basins; Irminger and Labrador basins.

Figure S4: Vertical profiles of pTE:^{234}Th and mineral:^{234}Th ratios in the upper 400m for the large size fraction (>53µm) along the GEOVIDE transect. There are three plots per element: Station #1 (shown alone because of the extreme values observed for few elements); Iberian, west European and Icelandic basins; Irminger and Labrador basins.

Figure S5: Concentration profiles of the pFe:pAl (mol/mol) and pFe:POC (mmol/mol) ratios, with the Eq depth (horizontal black dotted line), the pFe:pAl ratio in the UCC (vertical brown dashed line, from Taylor and McLenan, 1985) and the pFe:POC ratio in phytoplankton bulk (vertical green dashed line, from Twining et al., 2015). Ratios at Eq determined via the concentrations and the fluxes are indicated below each graph.

Table S1: Trace element concentrations (in nmol/L), mineral concentrations (in µg/L) and ^{234}Th activities (in dpm/L) for the large size fraction (>53µm) along the GEOVIDE transect.

The (*) indicate depths where POC was collected using a separate ISP unit, 10 to 50 m apart from the ISP dedicated to TEs.

Table S2: Particulate TE:^{234}Th (in nmol/dpm) and mineral:^{234}Th (in µg/dpm or ng/dpm) ratios in the large size fraction (>53µm), estimated at the Eq depth, along the GEOVIDE transect.

AUTHOR INFORMATION

Corresponding Author

* Nolwenn Lemaitre (nolwenn.lemaitre@erdw.ethz.ch)

Author Contributions

The manuscript was written through contributions of all authors. All authors have given approval to the final version of the manuscript.

Notes

The authors declare no competing financial interest.

ACKNOWLEDGEMENTS

We are grateful to the helpful captain and crew of the R/V Pourquoi Pas?, as well as to Fabien Perault and Emmanuel De Saint Léger from the CNRS DT-INSU who assisted during *in situ* pump deployments. Special thanks to Yi Tang (Queens College, USA), Virginie Sanial (WHOI, USA), Raphaëlle Sauzède (LOV, France) and Lorna Foliot (LSCE, France) for their help at sea and for the pump coordination and collaboration. We would also like to thank Phoebe Lam for providing two modified McLane ISP. Claire Bollinger from the Pôle Spectrométrie Océan (PSO, Brest, France) greatly helped during the element analysis by ICP-MS. We acknowledge Yoan Germain and Emmanuel Ponzevera for the use of the clean lab at IFREMER. Finally, we would like to thank the co-chief scientist Pascale Lherminier. This

work was funded by the French ANR Blanc GEOVIDE (ANR-13-BS06-0014), ANR RPDOC BITMAP (ANR-12-PDOC-0025-01), IFREMER, CNRS-INSU (programme LEFE), INSU OPTIMISP and Labex-Mer (ANR-10-LABX-19) and the Flanders Research Foundation (project G071512N) and Vrije Universiteit Brussel (Strategic Research Program, project SRP-2). Satellite chlorophyll a data and visualisations used in this study were produced with the Ocean Color (Ocean Biology Processing Group; OBPG) online data system, developed and maintained by NASA.

REFERENCES

(1) Morel, F. M. M.; Price, N. M. The Biogeochemical Cycles of Trace Metals in the Oceans. *Science (80-.).* **2003**, *300* (5621), 944–947. https://doi.org/10.1126/science.1083545.

(2) Sunda, W. Trace Metal Interactions with Marine Phytoplankton. *Biol. Oceanogr.* **1989**, *6*, 411–442. https://doi.org/10.1080/01965581.1988.10749543.

(3) Twining, B. S.; Baines, S. B. The Trace Metal Composition of Marine Phytoplankton. *Ann. Rev. Mar. Sci.* **2013**, *5*, 191–215. https://doi.org/10.1146/annurev-marine-121211-172322.

(4) Boyd, P. W.; Watson, a J.; Law, C. S.; Abraham, E. R.; Trull, T.; Murdoch, R.; Bakker, D. C.; Bowie, a R.; Buesseler, K. O.; Chang, H.; et al. A Mesoscale Phytoplankton Bloom in the Polar Southern Ocean Stimulated by Iron Fertilization. *Nature* **2000**, *407* (6805), 695–702. https://doi.org/10.1038/35037500.

(5) Moore, C. M.; Mills, M. M.; Arrigo, K. R.; Berman-Frank, I.; Bopp, L.; Boyd, P. W.; Galbraith, E. D.; Geider, R. J.; Guieu, C.; Jaccard, S. L.; et al. Processes and Patterns of Oceanic Nutrient Limitation. *Nat. Geosci.* **2013**, *6* (9), 701–710. https://doi.org/10.1038/ngeo1765.

(6) Martin, J. H. Glacial-Interglacial CO2 Change: The Iron Hypothesis. *Paleoceanography* **1990**, *5*, 1–13.

(7) Sigman, D. M.; Boyle, E. A. Glacial/Interglacial Variations in Atmospheric Carbon Dioxide. *Nature* **2000**, *407* (October), 859–869.

(8) Jickells, T. D.; Baker, A. R.; Chance, R. Atmospheric Transport of Trace Elements and Nutrients to the Oceans. *Philos. Trans. R. Soc. A* **2016**, *374*, 1–19. https://doi.org/10.1098/rsta.2015.0286.

(9) de Baar, H. J. W.; Jong, J. T. Distributions, Sources and Sinks of Iron in Seawater. *IUPAC Ser. analyitical Phys. Chem. Environ. Syst.* **2001**, *7*, 123–254.

(10) Jeandel, C. Overview of the Mechanisms That Could Explain the 'Boundary Exchange' at the Land–Ocean Contact. *Philos. Trans. R. Soc. A* **2016**, *374*. https://doi.org/10.1098/rsta.2015.0287.

(11) Homoky, W. B.; Weber, T.; Berelson, W. M.; Conway, T. M.; Henderson, G. M.; van Hulten, M.; Jeandel, C.; Severmann, S.; Tagliabue, A. Quantifying Trace Element and Isotope Fluxes at the Ocean–Sediment Boundary: A Review. *Philos. Trans. R. Soc. A*

2016, *374*. https://doi.org/10.1098/rsta.2016.0246.

(12) Goldberg, E. D. Chemical Scavengers of the Sea. *Chigaco Journals* **1954**, *62* (3), 249–265.

(13) Dehairs, F.; Chesselet, R.; Jedwab, J. Discrete Suspended Particles of Barite and the Barium Cycle in the Open Ocean. *Earth Planet. Sci. Lett.* **1980**, *49*, 528–550.

(14) Bishop, J. K. B. The Barite-Opal-Organic Carbon Association in Oceanic Particulate Matter. *Nature*. 1988, pp 341–343. https://doi.org/10.1038/332341a0.

(15) Ganeshram, R. S.; François, R.; Commeau, J.; Brown-Leger, S. L. An Experimental Investigation of Barite Formation in Seawater. *Geochim. Cosmochim. Acta* **2003**, *67* (14), 2599–2605. https://doi.org/10.1016/S0016-7037(03)00164-9.

(16) Bruland, K. W.; Lohan, M. C. Controls of Trace Metals in Seawater. In *The oceans and marine geochemistry*; Elderfield, H., Ed.; 2003; pp 23–47.

(17) Klaas, C.; Archer, D. E. Association of Sinking Organic Matter with Various Types of Mineral Ballast in the Deep Sea: Implications for the Rain Ratio. *Global Biogeochem. Cycles* **2002**, *16* (4), 1–14. https://doi.org/10.1029/2001GB001765.

(18) Lam, P. J.; Bishop, J. K. B. The Continental Margin Is a Key Source of Iron to the HNLC North Pacific Ocean. *Geophys. Res. Lett.* **2008**, *35* (7), 1–5. https://doi.org/10.1029/2008GL033294.

(19) Ohnemus, D. C.; Torrie, R.; Twining, B. S. Exposing the Distributions and Elemental Associations of Scavenged Particulate Phases in the Ocean Using Basin-Scale Multi-Element Data Sets. *Global Biogeochem. Cycles* **2019**, *33* (6), 725–748. https://doi.org/10.1029/2018GB006145.

(20) Puigcorbé, V.; Benitez-Nelson, C. R.; Masque, P.; Verdeny, E.; White, A.; Popp, B. N.; Prahl, F. G.; Lam, P. J. Small Phytoplankton Drive High Summertime Carbon and Nutrient Export in the Gulf of California and Eastern Tropical North Pacific. *Glob. Planet. Change* **2015**, *29*. https://doi.org/10.1002/2015GB005134.

(21) Giering, S. L. C.; Sanders, R.; Martin, A. P.; Lindemann, C.; Möller, K. O.; Daniels, C. J.; Mayor, D. J.; St. John, M. A. High Export via Small Particles before the Onset of the Nort Atlantic Spring Bloom. *J. Geophys. Res.* **2016**, *121*, 1–17. https://doi.org/10.1002/2016JC012048.Received.

(22) Fowler, S. W.; Knauer, G. a. Role of Large Particles in the Transport of Elements and Organic Compounds through the Oceanic Water Column. *Prog. Oceanogr.* **1986**, *16* (3), 147–194. https://doi.org/10.1016/0079-6611(86)90032-7.

(23) Frew, R. D.; Hutchins, D. A.; Nodder, S.; Sanudo-Wilhelmy, S.; Tovar-Sanchez, A.; Leblanc, K.; Hare, C. E.; Boyd, P. W. Particulate Iron Dynamics during FeCycle in Subantarctic Waters Southeast of New Zealand. *Global Biogeochem. Cycles* **2006**, *20* (1), 1–15. https://doi.org/10.1029/2005GB002558.

(24) Twining, B. S.; Nodder, S. D.; King, A. L.; Hutchins, D. A.; LeCleir, G. R.; DeBruyn, J. M.; Maas, E. W.; Vogt, S.; Wilhelm, S. W.; Boyd, P. W. Differential Remineralization of Major and Trace Elements in Sinking Diatoms. *Limnol. Oceanogr.* **2014**, *59* (3), 689–704. https://doi.org/10.4319/lo.2014.59.3.0689.

(25) Hayes, C. T.; Anderson, R. F.; Cheng, H.; Conway, T. M.; Edwards, R. L.; Fleisher, M. Q.; Ho, P.; Huang, K. F.; John, S. G.; Landing, W. M.; et al. Replacement Times of a Spectrum of Elements in the North Atlantic Based on Thorium Supply. *Global Biogeochem. Cycles* **2018**, *32* (9), 1294–1311. https://doi.org/10.1029/2017GB005839.

(26) Ellwood, M. J.; Nodder, S. D.; King, A. L.; Hutchins, D. A.; Wilhelm, S. W.; Boyd, P. W. Pelagic Iron Cycling during the Subtropical Spring Bloom, East of New Zealand. *Mar. Chem.* **2014**, *160* (MARCH), 18–33.

https://doi.org/10.1016/j.marchem.2014.01.004.

(27) Ho, T.; Chou, W.; Wei, C.; Lin, F.; Wong, G. T. F.; Lin, H.-L. Trace Metal Cycling in the Surface Water of the South China Sea: Vertical Fluxes, Composition, and Sources. *Limnol. Oceanogr.* **2010**, *55* (5), 1807–1820. https://doi.org/10.4319/lo.2010.55.5.1807.

(28) Kuss, J.; Waniek, J. J.; Kremling, K.; Schulz-bull, D. E. Seasonality of Particle-Associated Trace Element Fluxes in the Deep Northeast Atlantic Ocean. *Deep Sea Res. Part I Oceanogr. Res. Pap.* **2010**, *57* (6), 785–796. https://doi.org/10.1016/j.dsr.2010.04.002.

(29) Kuss, J.; Kremling, K. Particulate Trace Element Fluxes in the Deep Northeast Atlantic Ocean. *Deep Sea Res. Part I Oceanogr. Res. Pap.* **1999**, *46* (1), 149–169. https://doi.org/10.1016/S0967-0637(98)00059-4.

(30) Lamborg, C. H.; Buesseler, K. O.; Lam, P. J. Sinking Fluxes of Minor and Trace Elements in the North Pacific Ocean Measured during the VERTIGO Program. *Deep Sea Res. Part II Top. Stud. Oceanogr.* **2008**, *55* (14–15), 1564–1577. https://doi.org/10.1016/j.dsr2.2008.04.012.

(31) Lemaitre, N.; Planquette, H.; Dehairs, F.; van der Merwe, P.; Bowie, A. R.; Trull, T. W.; Laurenceau-Cornec, E. C.; Davies, D.; Bollinger, C.; Le Goff, M.; et al. Impact of the Natural Fe-Fertilization on the Magnitude, Stoichiometry and Efficiency of Particulate Biogenic Silica, Nitrogen and Iron Export Fluxes. *Deep. Res. Part I Oceanogr. Res. Pap.* **2016**, *117*, 11–27. https://doi.org/10.1016/j.dsr.2016.09.002.

(32) Planquette, H.; Sanders, R.; Statham, P. J.; Morris, P. J.; Fones, G. R. Fluxes of Particulate Iron from the Upper Ocean around the Crozet Islands: A Naturally Iron-Fertilized Environment in the Southern Ocean. *Global Biogeochem. Cycles* **2011**, *25* (2), 1–12. https://doi.org/10.1029/2010GB003789.

(33) Stanley, R. H. R.; Buesseler, K. O.; Manganini, S. J.; Steinberg, D. K.; Valdes, J. R. A Comparison of Major and Minor Elemental Fluxes Collected in Neutrally Buoyant and Surface-Tethered Sediment Traps. *Deep Sea Res. Part I Oceanogr. Res. Pap.* **2004**, *51*, 1387–1395. https://doi.org/10.1016/j.dsr.2004.05.010.

(34) Weinstein, S. E.; Moran, S. B. Vertical Flux of Particulate Al, Fe, Pb, and Ba from the Upper Ocean Estimated from 234Th/238U Disequilibria. *Deep Sea Res. Part I Oceanogr. Res. Pap.* **2005**, *52* (8), 1477–1488. https://doi.org/http://dx.doi.org/10.1016/j.dsr.2005.03.008.

(35) Black, E. E.; Kienast, S. S.; Lemaitre, N.; Lam, P. J.; Anderson, R. F.; Planquette, H.; Planchon, F.; Buesseler, K. O. Ironing out Fe Residence Time in the Dynamic Upper Ocean. *Global Biogeochem. Cycles* **2020**, *34*, 1–17. https://doi.org/10.1029/2020GB006592.

(36) Black, E. E.; Lam, P. J.; Lee, J. M.; Buesseler, K. O. Insights from the 238U- 234Th Method into the Coupling of Biological Export and the Cycling of Cadmium, Cobalt, and Manganese in the Southeast Pacific Ocean. *Global Biogeochem. Cycles* **2019**, *33* (1), 15–36. https://doi.org/10.1029/2018GB005985.

(37) Benitez-Nelson, C. R.; Bidigare, R.; Dickey, T. D.; Landry, M. R.; Leonard, C. L.; Brown, S. L.; Nencioli, F.; Rii, Y. M.; Maiti, K.; Becker, J. W.; et al. Mesoscale Eddies Drive Increased Silica Export in the Subtropical Pacific Ocean. *Science (80-.).* **2007**, *316*, 1017–1022. https://doi.org/10.1126/science.1136221.

(38) Conte, M. H.; Carter, A. M.; Koweek, D. A.; Huang, S.; Weber, J. C. The Elemental Composition of the Deep Particle Flux in the Sargasso Sea. *Chem. Geol.* **2019**, *511* (October 2018), 279–313. https://doi.org/10.1016/j.chemgeo.2018.11.001.

(39) McDonnell, A. M. P.; Lam, P. J.; Lamborg, C. H.; Buesseler, K. O.; Sanders, R.; Riley, J. S.; Marsay, C.; Smith, H. E. K.; Sargent, E. C.; Lampitt, R. S.; et al. The Oceanographic Toolbox for the Collection of Sinking and Suspended Marine Particles. *Prog. Oceanogr.* **2015**, *133*, 17–31. https://doi.org/10.1016/j.pocean.2015.01.007.

(40) Coale, K. H.; Bruland, K. W. Thorium-234:Uranium-238 Disequilibria within the California Current. *Limnol. Oceanogr.* **1985**, *30* (l), 22–33. https://doi.org/10.4319/lo.1985.30.1.0022.

(41) Buesseler, K. O.; Bacon, M. P.; Kirk Cochran, J.; Livingston, H. D. Carbon and Nitrogen Export during the JGOFS North Atlantic Bloom Experiment Estimated from 234Th: 238U Disequilibria. *Deep Sea Res. Part A. Oceanogr. Res. Pap.* **1992**, *39* (7–8), 1115–1137. https://doi.org/10.1016/0198-0149(92)90060-7.

(42) Cochran, J. K.; Masqué, P. Short-Lived U/Th Series Radionuclides in the Ocean: Tracers for Scavenging Rates, Export Fluxes and Particle Dynamics. *Rev. Mineral. Geochemistry* **2003**, *52*, 461–492. https://doi.org/10.2113/0520461.

(43) Kuss, J.; Kremling, K. Spatial Variability of Particle Associated Trace Elements in Near-Surface Waters of the North Atlantic (30°N/60°W to 60°N/2°W), Derived by Large Volume Sampling. *Mar. Chem.* **1999**, *68* (1–2), 71–86. https://doi.org/10.1016/S0304-4203(99)00066-3.

(44) Ohnemus, D. C.; Lam, P. J. Cycling of Lithogenic Marine Particulates in the US GEOTRACES North Atlantic Transect. *Deep Sea Res. Part II Top. Stud. Oceanogr.* **2014**, *116* (November 2015), 283–302. https://doi.org/http://dx.doi.org/10.1016/j.dsr2.2014.11.019.

(45) Pohl, C.; Croot, P. L.; Hennings, U.; Daberkow, T.; Budeus, G.; Rutgers van der Loeff, M. M. Synoptic Transects on the Distribution of Trace Elements (Hg, Pb, Cd, Cu, Ni, Zn, Co, Mn, Fe, and Al) in Surface Waters of the Northern- and Southern East Atlantic. *J. Mar. Syst.* **2011**, *84* (1–2), 28–41. https://doi.org/10.1016/j.jmarsys.2010.08.003.

(46) Saito, M. A.; Noble, A. E.; Hawco, N.; Twining, B. S.; Ohnemus, D. C.; John, S. G.; Lam, P.; Conway, T. M.; Johnson, R.; Moran, D.; et al. The Acceleration of Dissolved Cobalt's Ecological Stoichiometry Due to Biological Uptake, Remineralization, and Scavenging in the Atlantic Ocean. *Biogeosciences* **2017**, *14* (20), 4637–4662. https://doi.org/10.5194/bg-14-4637-2017.

(47) Weinstein, S. E.; Moran, S. B. Distribution of Size-Fractionated Particulate Trace Metals Collected by Bottles and in-Situ Pumps in the Gulf of Maine-Scotian Shelf and Labrador Sea. *Mar. Chem.* **2004**, *87* (3–4), 121–135. https://doi.org/10.1016/j.marchem.2004.02.004.

(48) Nielsdottir, M. C.; Moore, C. M.; Sanders, R.; Hinz, D. J.; Achterberg, E. P. Iron Limitation of the Postbloom Phytoplankton Communities in the Iceland Basin. *Global Biogeochem. Cycles* **2009**, *23*, 1–13. https://doi.org/10.1029/2008GB003410.

(49) Achterberg, E. P.; Moore, C. M.; Henson, S. A.; Steigenberger, S.; Stohl, A.; Eckhardt, S.; Avendano, L. C.; Cassidy, M.; Hembury, D.; Klar, J. K.; et al. Natural Iron Fertilization by the Eyjafjallajökull Volcanic Eruption. *Geophys. Res. Lett.* **2013**, *40*, 921–926. https://doi.org/10.1002/grl.50221.

(50) Blain, S.; Guieu, C.; Claustre, H.; Leblanc, K.; Moutin, T.; Guiner, B. Q.; Ras, J.; Sarthou, G. Availability of Iron and Major Nutrients for Phytoplankton in the North-East Atlantic Ocean. *Limnol. Oceanogr.* **2004**, *49* (6), 2095–2104. https://doi.org/10.4319/lo.2004.49.6.2095.

(51) Moore, C. M.; Mills, M. M.; Langlois, R.; Milne, A.; Achterberg, E. P.; Roche, J. La;

Geider, R. J. Relative Influence of Nitrogen and Phosphorus Availability on Phytoplankton Physiology and Productivity in the Oligotrophic Sub-Tropical North Atlantic Ocean. *Limnol. Oceanogr.* **2008**, *53* (1), 291–305.

(52) Owens, S. A.; Pike, S.; Buesseler, K. O. Thorium-234 as a Tracer of Particle Dynamics and Upper Ocean Export in the Atlantic Ocean. *Deep Sea Res. Part II Top. Stud. Oceanogr.* **2014**, *116*, 42–59. https://doi.org/10.1016/j.dsr2.2014.11.010.

(53) Thomalla, S.; Turnewitsch, R.; Lucas, M.; Poulton, A. Particulate Organic Carbon Export from the North and South Atlantic Gyres: The 234Th/238U Disequilibrium Approach. *Deep Sea Res. Part II Top. Stud. Oceanogr.* **2006**, *53*, 1629–1648. https://doi.org/10.1016/j.dsr2.2006.05.018.

(54) Antia, N.; Peinert, R.; Hebbeln, D.; Bathmann, U.; Fehner, U.; Zeitzschel, B. Basin-Wide Particulate Carbon Flux in the Atlantic Ocean ' Regional Export Patterns and Potential for Atmospheric Sequestration Avan Detlef TM Jan s Susanne Regional Differences in Changes of the Export Ratio with Depth Are Related to over the Atlantic Oc. *Global Biogeochem. Cycles* **2001**, *15* (4), 845–862. https://doi.org/10.1029/2000gb001376.

(55) Billet, D. S. M.; Lampitt, R. S.; Rice, A. L.; Mantoura, R. F. C. Seasonal Sedimentation of Phytoplankton to the Deep-Sea Benthos. *Nature* **1983**, *302*.

(56) Henson, S. A.; Dunne, J. P.; Sarmiento, J. L. Decadal Variability in North Atlantic Phytoplankton Blooms. *J. Geophys. Res.* **2009**, *114* (C4), C04013–C04013. https://doi.org/10.1029/2008JC005139.

(57) Lampitt, R. S.; Salter, I.; de Cuevas, B. A.; Hartman, S.; Larkin, K. E.; Pebody, C. A. Long-Term Variability of Downward Particle Flux in the Deep Northeast Atlantic: Causes and Trends. *Deep Sea Res. Part II Top. Stud. Oceanogr.* **2010**, *57* (15), 1346–1361. https://doi.org/10.1016/j.dsr2.2010.01.011.

(58) Peinert, R.; Antia, A. N.; Bauerfeind, E.; v. Bodungen, B.; Haupt, O.; Krumbholz, M.; Peeken, I.; Ramseier, R. O.; Voss, M.; Zeitzschel, B. Particle Flux Variability in the Polar and Atlantie Biogeoehemieal Provinees of the Nordie Seas. *North. North Atl.* **2001**, 53–68.

(59) Lam, P. J.; Ohnemus, D. C.; Auro, M. E. Size-Fractionated Major Particle Composition and Concentrations from the US GEOTRACES North Atlantic Zonal Transect. *Deep Sea Res. Part II Top. Stud. Oceanogr.* **2015**, *116*, 303–320. https://doi.org/10.1016/j.dsr2.2014.11.020.

(60) Lemaitre, N.; Planchon, F.; Planquette, H.; Dehairs, F.; Fonseca-Batista, D.; Roukaerts, A.; Deman, F.; Mariez, C.; Sarthou, G. High Variability of Export Fluxes along the North Atlantic GEOTRACES Section GA01: Particulate Organic Carbon Export Deduced from the 234Th Method. *Biogeosciences* **2018**, *15* (21), 6417–6437. https://doi.org/10.5194/bg-15-2289-2018.

(61) Fonseca-Batista, D.; Li, X.; Riou, V.; Michotey, V.; Deman, F.; Fripiat, F.; Guasco, S.; Brion, N.; Lemaitre, N.; Tonnard, M.; et al. Evidence of High N2 Fixation Rates in the Temperate Northeast Atlantic. *Biogeosciences* **2019**, *16*, 999–1017. https://doi.org/10.5194/bg-16-999-2019.

(62) Tonnard, M. Etude Du Cycle Biogéochimique Du Fer : Distribution et Spéciation Dans l'océan Atlantique Nord (GA01) et l'océan Austral (GIpr05) (GEOTRACES), Université de Bretagne Occidentale & Université de Tasmanie, 2018.

(63) Pike, S.; Buesseler, K. O.; Andrews, J.; Savoye, N. Quantification of 234Th Recovery in Small Volume Seawater Samples by Inductively Coupled Plasma Mass Spectrometry. *J. Radioanal. Nucl. Chem.* **2005**, *263*, 355–360.

(64) Savoye, N.; Benitez-Nelson, C.; Burd, A. B.; Cochran, J. K.; Charette, M.; Buesseler, K. O.; Jackson, G. A.; Roy-Barman, M.; Schmidt, S.; Elskens, M. 234Th Sorption and Export Models in the Water Column: A Review. *Mar. Chem.* **2006**, *100*, 234–249. https://doi.org/10.1016/j.marchem.2005.10.014.

(65) Gourain, A.; Planquette, H.; Cheize, M.; Lemaitre, N.; Menzel Barraqueta, J. L.; Shelley, R.; Lherminier, P.; Planquette, H. Inputs and Processes Affecting the Distribution of Particulate Iron in the North Atlantic along the GEOVIDE (GEOTRACES GA01) Section. *Biogeosciences* **2019**, *16* (7), 1563–1582. https://doi.org/10.5194/bg-16-1563-2019.

(66) Planquette, H.; Sherrell, R. M. Sampling for Particulate Trace Element Determination Using Water Sampling Bottles: Methodology and Comparison to in Situ Pumps. *Limnol. Oceanogr. Methods* **2012**, *10*, 367–388. https://doi.org/10.4319/lom.2012.10.367.

(67) Taylor, S. R.; Mclennan, S. M. *The Continental Crust: Its Composition and Evolution*, Blackwell,.; 1985.

(68) Moran, S. B.; Moore, R. M. Evidence from Mesocosm Studies for Biological Removal of Dissolved Aluminium from Sea Water. *Nature* **1988**, *335* (6192), 706–708. https://doi.org/10.1038/335706a0.

(69) Menzel Barraqueta, J.-L.; Schlosser, C.; Planquette, H.; Gourain, A.; Cheize, M.; Boutorh, J.; Shelley, R.; Pereira Contraira, L.; Gledhill, M.; Hopwood, M. J.; et al. Aluminium in the North Atlantic Ocean and the Labrador Sea (GEOTRACES GA01 Section): Roles of Continental Inputs and Biogenic Particle Removal. *Biogeosciences* **2018**, *15*, 5271–5286. https://doi.org/10.5194/bg-15-5271-2018.

(70) Lam, P. J.; Lee, J. M.; Heller, M. I.; Mehic, S.; Xiang, Y.; Bates, N. R. Size-Fractionated Distributions of Suspended Particle Concentration and Major Phase Composition from the U.S. GEOTRACES Eastern Pacific Zonal Transect (GP16). *Mar. Chem.* **2018**, *201* (April), 90–107. https://doi.org/10.1016/j.marchem.2017.08.013.

(71) Twining, B. S.; Rauschenberg, S.; Morton, P. L.; Vogt, S. Metal Contents of Phytoplankton and Labile Particulate Material in the North Atlantic Ocean. *Prog. Oceanogr.* **2015**, *137*, 261–283. https://doi.org/10.1016/j.pocean.2015.07.001.

(72) Broecker, W.; Peng, T. *Tracers in the Sea*, Lamont-Doh.; 1982.

(73) Ragueneau, O.; Savoye, N.; Del Amo, Y.; Cotten, J.; Tardiveau, B.; Leynaert, A. A New Method for the Measurement of Biogenic Silica in Suspended Matter of Coastal Waters: Using Si:Al Ratios to Correct for the Mineral Interference. *Cont. Shelf Res.* **2005**, *25* (5–6), 697–710. https://doi.org/10.1016/j.csr.2004.09.017.

(74) Aminot, A.; Kérouel, R. *Dosage Automatique Des Nutriments Dans Les Eaux Marines: Méthodes En Flux Continu*, Ifremer-Qu.; 2007.

(75) Hydes, D. J.; Liss, P. S. Fluorimetric Method for the Determination of Low Concentrations of Dissolved Aluminium in Natural Waters. *Analyst* **1976**, *101*, 922–931.

(76) Mortlock, R. A.; Froelich, P. N. A Simple Method for the Rapid Determination of Biogenic Opal in Pelagic Marine Sediments. *Deep Sea Res. Part A, Oceanogr. Res. Pap.* **1989**, *36* (9), 1415–1426. https://doi.org/10.1016/0198-0149(89)90092-7.

(77) Bishop, J. K. B.; Edmond, J. M.; Ketten, D. R.; Bacon, M. P.; Silker, W. B. The Chemistry, Biology and Vertical Flux of Particulate Matter from the Upper 400m of the Equatorial Atlantic Ocean. *Deep Sea Res. Part A, Oceanogr. Res. Pap.* **1977**, *24* (6), 511–548.

(78) Michaels, A. F.; Silver, M. W. Primary Production, Sinking Fluxes and the Microbial Food Web. *Deep Sea Res. Part A. Oceanogr. Res. Pap.* **1988**, *35* (4), 473–490.

(79) Villa-Alfageme, M.; Soto, F. C.; Ceballos, E.; Giering, S. L. C.; Le Moigne, F. A. C.; Henson, S.; Mas, J. L.; Sanders, R. J. Geographical, Seasonal and Depth Variation in Sinking Particle Speeds in the North Atlantic. *Geophys. Res. Lett.* **2016**, *43*, 8609–8616. https://doi.org/10.1002/2016GL069233.Received.

(80) Le Moigne, F. A. C.; Villa-Alfageme, M.; Sanders, R. J.; Marsay, C.; Henson, S.; García-Tenorio, R. Export of Organic Carbon and Biominerals Derived from 234Th and 210Po at the Porcupine Abyssal Plain. *Deep Sea Res. Part I Oceanogr. Res. Pap.* **2013**, *72* (August), 88–101. https://doi.org/10.1016/j.dsr.2012.10.010.

(81) Planchon, F.; Ballas, D.; Cavagna, A.-J.; Bowie, A. R.; Davies, D. M.; Trull, T.; Laurenceau, E. C.; van der Merwe, P.; Dehairs, F. Carbon Export in the Naturally Iron-Fertilized Kerguelen Area of the Southern Ocean Based on the 234 Th Approach. *Biogeosciences* **2015**, *12*, 3831–3848. https://doi.org/10.5194/bgd-12-3831-2015.

(82) Puigcorbé, V.; Roca-Martí, M.; Masqué, P.; Benitez-Nelson, C.; Rutgers van der Loeff, M.; Bracher, A.; Moreau, S. Latitudinal Distributions of Particulate Carbon Export across the North Western Atlantic Ocean. *Deep Sea Res. Part I Oceanogr. Res. Pap.* **2017**. https://doi.org/10.1016/j.dsr.2017.08.016.

(83) Black, E. E.; Buesseler, K. O.; Pike, S. M.; Lam, P. J. 234Th as a Tracer of Particulate Export and Remineralization in the Southeastern Tropical Pacific. *Mar. Chem.* **2018**, *201*, 35–50. https://doi.org/10.1016/j.marchem.2017.06.009.

(84) Durkin, C. A.; Estapa, M. L.; Buesseler, K. O. Observations of Carbon Export by Small Sinking Particles in the Upper Mesopelagic. *Mar. Chem.* **2015**, *175*, 72–81. https://doi.org/10.1016/j.marchem.2015.02.011.

(85) Tonnard, M.; Planquette, H.; Bowie, A. R.; van der Merwe, P.; Gallinari, M.; Desprez de Gésincourt, F.; Germain, Y.; Gourain, A.; Benetti, M.; Reverdin, G.; et al. Dissolved Iron in the North Atlantic Ocean and Labrador Sea along the GEOVIDE Section (GEOTRACES Section GA01). *Biogeosciences* **2020**, *14*, 917–943. https://doi.org/10.5194/bg-17-917-2020.

(86) Planquette, H.; Fones, G. R.; Statham, P. J.; Morris, P. J. Origin of Iron and Aluminium in Large Particles (> 53 Mm) in the Crozet Region, Southern Ocean. *Mar. Chem.* **2009**, *115* (1–2), 31–42. https://doi.org/DOI 10.1016/j.marchem.2009.06.002.

(87) Schlitzer, R.; Anderson, R. F.; Masferrer Dodas, E.; Lohan, M. C.; Geibert, W.; Tagliabue, A.; Bowie, A. R.; Jeandel, C.; Maldonado, M. T.; Landing, W. M.; et al. The GEOTRACES Intermediate Data Product 2017. *Chem. Geol.* **2018**, *493* (June), 210–223. https://doi.org/10.1016/j.chemgeo.2018.05.040.

(88) Smith, J. N.; Yeats, P. A.; Knowlton, S. E.; Moran, S. B. Comparison of 234Th/238U and Mass Balance Models for Estimating Metal Removal Fluxes in the Gulf of Maine and Scotian Shelf. *Cont. Shelf Res.* **2014**, *77*, 107–117. https://doi.org/10.1016/j.csr.2014.01.008.

(89) Buesseler, K. O.; Benitez-Nelson, C. R.; Moran, S. B.; Burd, a.; Charette, M.; Cochran, J. K.; Coppola, L.; Fisher, N. S.; Fowler, S. W.; Gardner, W. D.; et al. An Assessment of Particulate Organic Carbon to Thorium-234 Ratios in the Ocean and Their Impact on the Application of 234Th as a POC Flux Proxy. *Mar. Chem.* **2006**, *100* (3-4 SPEC. ISS.), 213–233. https://doi.org/10.1016/j.marchem.2005.10.013.

(90) Shelley, R. U.; Roca-Martí, M.; Castrillejo, M.; Masqué, P.; Landing, W. M.; Planquette, H.; Sarthou, G. Quantification of Trace Element Atmospheric Deposition Fluxes to the Atlantic Ocean (>40°N; GEOVIDE, GEOTRACES GA01) during Spring

2014. *Deep. Res. Part I Oceanogr. Res. Pap.* **2017**, *119* (November), 34–49. https://doi.org/10.1016/j.dsr.2016.11.010.

(91) Leinen, M.; Pisias, N. An Objective Technique for Determining End-Member Compositions and for Partitioning Sediments According to Their Sources. *Geochim. Cosmochim. Acta* **1984**, *48* (1), 47–62. https://doi.org/10.1016/0016-7037(84)90348-X.

(92) Templ, M.; Filzmoser, P.; Reimann, C. Cluster Analysis Applied to Regional Geochemical Data: Problems and Possibilities. *Appl. Geochemistry* **2008**, *23* (8), 2198–2213. https://doi.org/10.1016/j.apgeochem.2008.03.004.

(93) Takematsu, N. Sorption of Transition Metals on Manganese and Iron Oxides, and Solicate Minerals. *J. Oceanogr. Soc. Japan* **1979**, *35*, 36–42.

(94) Duarte, B.; Caçador, I. Particulate Metal Distribution in Tagus Estuary (Portugal) during a Flood Episode. *Mar. Pollut. Bull.* **2012**, *64* (10), 2109–2116. https://doi.org/10.1016/j.marpolbul.2012.07.016.

(95) Cotté-Krief, M.-H.; Guieu, C.; Thomas, A. J.; Martin, J.-M. Sources of Cd, Cu, Ni and Zn in Portuguese Coastal Waters. *Mar. Chem.* **2000**, *71*, 199–214.

(96) Duarte, B.; Silva, G.; Lino, J.; Paulo, J.; Azeda, C.; Sá, E.; Metelo, I.; José, M.; Caçador, I. Heavy Metal Distribution and Partitioning in the Vicinity of the Discharge Areas of Lisbon Drainage Basins (Tagus Estuary , Portugal). *J. Sea Res.* **2014**, *93*, 101–111. https://doi.org/10.1016/j.seares.2014.01.003.

(97) Caçador, I.; Vale, C.; Catarino, F. Accumulation of Zn, Pb, Cu, Cr and Ni in Sediments between Roots of the Tagus Estuary Salt Marshes, Portugal. *Estuar. Coast. Shelf Sci.* **1996**, *42*, 393–403.

(98) Le Gall, A. C.; Statham, P. J.; Morley, N. J.; Hydes, D. J.; Hunt, C. H. Processes Influencing Distributions and Concentrations of Cd, Cu, Mn and Ni at the North West European Shelf Break. *Mar. Chem.* **1999**, *68*, 97–115.

(99) Ye, Y.; Völker, C. On the Role of Dust-Deposited Lithogenic Particles for Iron Cycling in the Tropical and Subtropical Atlantic. *Global Biogeochem. Cycles* **2017**, *31* (10), 1543–1558. https://doi.org/10.1002/2017GB005663.

(100) Tagliabue, A.; Bowie, A. R.; Boyd, P. W.; Buck, K. N.; Johnson, K. S.; Saito, M. A. The Integral Role of Iron in Ocean Biogeochemistry. *Nature* **2017**, *543* (7643), 51–59. https://doi.org/10.1038/nature21058.

(101) Lagarde, M.; Lemaitre, N.; Planquette, H.; Grenier, M.; Belhadj, M.; Jeandel, C. Particulate Rare Earth Element Behavior in the North Atlantic (GEOVIDE Cruise). *Biogeosciences Discuss.* **2020**, No. January, 1–32. https://doi.org/10.5194/bg-2019-462.

(102) van Weering, T. C. E.; de Stigter, H. C.; Boer, W.; de Haas, H. Recent Sediment Transport and Accumulation on the NW Iberian Margin. *Prog. Earth Planet. Sci.* **2002**, *52*, 349–371.

(103) McCave, I. N.; Hall, I. R. Turbidity of Waters over the Northwest Iberian Continental Margin. *Prog. Oceanogr.* **2002**, *52* (2–4), 299–313. https://doi.org/10.1016/S0079-6611(02)00012-5.

(104) Moffett, J. W.; Ho, J. Oxidation of Cobalt and Manganese in Seawater via a Common Microbially Catalyzed Pathway. *Geochim. Cosmochim. Acta* **1996**, *60* (18), 3415–3424.

(105) Zunino, P.; Lherminier, P.; Mercier, H.; Daniault, N.; García-Ibáñez, M. I.; Pérez, F. F. The GEOVIDE Cruise in May-June 2014 Reveals an Intense Meridional Overturning Circulation over a Cold and Fresh Subpolar North Atlantic. *Biogeosciences* **2017**, *14*

(23), 5323–5342. https://doi.org/10.5194/bg-14-5323-2017.

(106) Van Hulten, M.; Middag, R.; Dutay, J. C.; De Baar, H.; Roy-Barman, M.; Gehlen, M.; Tagliabue, A.; Sterl, A. Manganese in the West Atlantic Ocean in the Context of the First Global Ocean Circulation Model of Manganese. *Biogeosciences* **2017**, *14* (5), 1123–1152. https://doi.org/10.5194/bg-14-1123-2017.

(107) John, S. G.; Conway, T. M. A Role for Scavenging in the Marine Biogeochemical Cycling of Zinc and Zinc Isotopes. *Earth Planet. Sci. Lett.* **2014**, *394*, 159–167. https://doi.org/10.1016/j.epsl.2014.02.053.

(108) Twining, B. S.; Rauschenberg, S.; Morton, P. L.; Ohnemus, D. C.; Lam, P. J. Comparison of Particulate Trace Element Concentrations in the North Atlantic Ocean as Determined with Discrete Bottle Sampling and in Situ Pumping. *Deep Sea Res. Part II Top. Stud. Oceanogr.* **2015**, *116*, 273–282. https://doi.org/10.1016/j.dsr2.2014.11.005.

(109) Collier, R.; Edmond, J. The Trace Element Geochemistry of Marine Biogenic Particulate Matter. *Prog. Oceanogr.* **1984**, *13*, 113–199.

(110) King, a. L.; Sañudo-Wilhelmy, S. a.; Boyd, P. W.; Twining, B. S.; Wilhelm, S. W.; Breene, C.; Ellwood, M. J.; Hutchins, D. a. A Comparison of Biogenic Iron Quotas during a Diatom Spring Bloom Using Multiple Approaches. *Biogeosciences* **2012**, *9* (2), 667–687. https://doi.org/10.5194/bg-9-667-2012.

(111) Muggli, D. L.; Harrison, P. J. Effects of Nitrogen Source on the Physiology and Metal Nutrition of Emiliania Huxleyi Grown under Different Iron and Light Conditions. *Mar. Ecol. Prog. Ser.* **1996**, *130* (Raven 1988), 255–267.

(112) Muggli, D. L.; Lecourt, M.; Harrison, P. J. Effects of Iron and Nitrogen Source on the Sinking Rate , Physiology and Metal Composition of an Oceanic Diatom from the Subarctic Pacific. *Mar. Ecol. Prog. Ser.* **1996**, *132*, 215–227.

(113) Sunda, W. G.; Huntsman, S. A. Iron Uptake and Growth Limitation in Oceanic and Coastal Phytoplankton. *Mar. Chem.* **1995**, *50*, 189–206.

(114) Lemaitre, N.; Planquette, H.; Planchon, F.; Sarthou, G.; Jacquet, S.; García-Ibáñez, M. I.; Gourain, A.; Cheize, M.; Monin, L.; André, L.; et al. Particulate Barium Tracing Significant Mesopelagic Carbon Remineralisation in the North Atlantic. *Biogeosciences* **2018**, *15*, 2289–2307. https://doi.org/10.5194/bg-15-2289-2018.

(115) Boiteau, R. M.; Mende, D. R.; Hawco, N. J.; McIlvin, M. R.; Fitzsimmons, J. N.; Saito, M. A.; Sedwick, P. N.; Delong, E. F.; Repeta, D. J. Siderophore-Based Microbial Adaptations to Iron Scarcity across the Eastern Pacific Ocean. *Proc. Natl. Acad. Sci. U. S. A.* **2016**, *113* (50), 14237–14242. https://doi.org/10.1073/pnas.1608594113.

(116) Maerz, J.; Six, K. D.; Stemmler, I.; Ahmerkamp, S.; Ilyina, T. Microstructure and Composition of Marine Aggregates as Co-Determinants for Vertical Particulate Organic Carbon Transfer in the Global Ocean. *Biogeosciences* **2020**, *17* (7), 1765–1803. https://doi.org/10.5194/bg-17-1765-2020.

(117) García-Ibáñez, M. I.; Pérez, F. F.; Lherminier, P.; Zunino, P.; Mercier, H.; Tréguer, P. Water Mass Distributions and Transports for the 2014 GEOVIDE Cruise in the North Atlantic. *Biogeosciences* **2018**, *15* (7), 2075–2090. https://doi.org/10.5194/bg-15-2075-2018.